# PHASE EQUILIBRIA OF BINARY SYSTEMS WITH CARBON DIOXIDE AND CARBON DIOXIDE-PHILIC MATERIALS

A THESIS SUBMITTED TO
THE GRADUATE SCHOOL OF NATURAL AND APPLIED SCIENCES
OF
MIDDLE EAST TECHNICAL UNIVERSITY

BY

BERIL DUMANLILAR

IN PARTIAL FULFILLMENT OF THE REQUIREMENTS
FOR
THE DEGREE OF MASTER OF SCIENCE
IN
CHEMICAL ENGINEERING

JULY 2019

Approval of the thesis:

# PHASE EQUILIBRIA OF BINARY SYSTEMS WITH CARBON DIOXIDE AND CARBON DIOXIDE-PHILIC MATERIALS

submitted by **BERIL DUMANLILAR** in partial fulfillment of the requirements for the degree of **Master of Science in Chemical Engineering Department, Middle East Technical University** by,

Prof. Dr. Halil Kalıpçılar
Dean, Graduate School of **Natural and Applied Sciences**

Prof. Dr. Pınar Çalık
Head of Department, **Chemical Engineering**

Assoc. Prof. Dr. Çerağ Dilek Hacıhabiboğlu
Supervisor, **Chemical Engineering, METU**

**Examining Committee Members:**

Prof. Dr. Halil Kalıpçılar
Chemical Engineering Dept., METU

Assoc. Prof. Dr. Çerağ Dilek Hacıhabiboğlu
Chemical Engineering, METU

Prof. Dr. Özkan Murat Doğan
Chemical Engineering Dept., Gazi Uni.

Prof. Dr. Levent Yılmaz
Chemical Engineering Dept., METU

Prof. Dr. Yusuf Uludağ
Chemical Engineering Dept., METU

Date: 18.07.2019

**I hereby declare that all information in this document has been obtained and presented in accordance with academic rules and ethical conduct. I also declare that, as required by these rules and conduct, I have fully cited and referenced all material and results that are not original to this work.**

Name, Surname: Beril Dumanlılar

Signature:

# ABSTRACT

## PHASE EQUILIBRIA OF BINARY SYSTEMS WITH CARBON DIOXIDE AND CARBON DIOXIDE-PHILIC MATERIALS

Dumanlılar, Beril
Master of Science, Chemical Engineering
Supervisor: Assoc. Prof. Dr. Çerağ Dilek Hacıhabiboğlu

July 2019, 77 pages

Phase behavior investigations in supercritical carbon dioxide (scCO$_2$) permit design and development of new and environmentally friendly supercritical fluid processes. Recently polyhedral oligomeric silsesquioxanes (POSS) modified with certain functional groups have been found to be soluble in supercritical CO$_2$. In this thesis, solubilities of methacrylisobutyl POSS (MIBPOSS) and methacrylisooctyl POSS (MIOPOSS) in scCO$_2$ have been studied. In the structure of these molecules, one of the eight branched alkyl chain functionalities attached to the Si atoms of the cage structure has been replaced with a CO$_2$-philic functional group, methacryl, to improve the enthalpic contribution on their solubility. The cloud or dew points were determined using a high-pressure visible cell at the temperature range of 308-323 K, up to 22.1 MPa. The measured highest solubility of MIBPOSS was 0.006 mol fr. at 323 K and 16.8 MPa, while it was 0.0017 mol fr. at 323 K and 22.1 MPa for MIOPOSS. Both MIBPOSS and MIOPOSS exhibit higher solubilities in scCO$_2$ compared to their counterparts with single type of functionality, octaisobutyl POSS, isooctyl POSS and methacryl POSS. The solubility data were modeled by using six different density-based semi-empirical models, all of which give good correlations. One interesting feature that was observed in the phase behavior studies of the MIBPOSS-CO$_2$ binary system was pressure-induced melting temperature (MT) depression of POSS. The maximum measured decrease in the MT was 77 K degrees under the $CO_2$ pressure of 4.8 MPa. Beside these studies, a model was developed to predict the MT depression of various $CO_2$-philic aromatic molecules including naphthalene, biphenyl and 1, 3, 5-tri-terbutylbenzene (TTBB) in $CO_2$, which sufficiently predicted their MT depression behavior.

Keywords: POSS, Supercritical Carbon Dioxide, Phase Behavior, Solubility, Density Based Models

# ÖZ

# KARBONDİOKSİT VE KARBONDİOKSİTLE UYUMLU MADDELERİ İÇEREN İKİLİ SİSTEMLERİN FAZ DENGESİ

Dumanlılar, Beril
Yüksek Lisans, Kimya Mühendisliği
Tez Danışmanı: Doç. Dr. Çerağ Dilek Hacıhabiboğlu

Temmuz 2019, 77 sayfa

Süperkritik karbondioksit (sk$CO_2$) içerisindeki maddelerin, çözünürlük ve faz dengesi çalışmaları yeni çevre dostu süperkritik akışkan prosesleri tasarlanmasına ve bu proseslerin geliştirilmesine olanak sağlamaktadır. Yakın zamanda bazı fonskiyonel gruplarla donatılmış polihedral oligomerik silseskuioksanların (POSS) süperkritik $CO_2$'de (sk$CO_2$) çözünür olduğu bulunmuştur. Bu tezde metakrilizobutil POSS (MIBPOSS) ve metakrilizooktil POSS (MIOPOSS)'un sk$CO_2$'de çözünürlükleri çalışılmıştır. Bu moleküllerin yapısında, kafes yapıdaki Si atomuna bağlı sekiz dallı alkil grubundan biri bu maddelerin çözünürlükleri üzerindeki entalpik katkıyı artırmak için $CO_2$-uyumlu bir fonksiyonel grup olan metakril grubu ile değiştirilmiştir. Bulutlanma ya da çiğlenme noktaları gözlemlenebilir yüksek basınç hücresi kullanılarak 308-323 K sıcaklık aralığında 22.1 MPa'a kadar belirlenmiştir. MIBPOSS'un ölçülmüş olan en yüksek çözünürlüğü 323 K ve 16.8 MPa'da 0.006 mol kesri iken MIOPOSS için bu değer 323 K ve 22.1 MPa'da 0.0017 mol kesridir. MIBPOSS ve MIOPOSS, tek çeşit fonksiyonel grubu içeren benzerleri olan oktaizobütil POSS, isooktil POSS ve metakril POSS'a göre sk$CO_2$ içerisinde daha yüksek çözünürlük sergilemişlerdir. Çözünürlük verileri altı farklı yarı deneysel yoğunluk temelli korelasyonlar kullanılarak modellenmiş ve hepsi iyi seviyede korelasyon vermiştir. MIBPOSS-$CO_2$ ikili sistemin faz dengesi çalışması sırasında farklı olarak, yüksek basınçtan kaynaklanan, erime sıcaklığında düşüş gözlenmiştir. Ölçülen maksimum erime sıcaklığı düşmesi 4.8 MPa’da 77 K’dir. Bu çalışmalara ek olarak, naftalin, bifenil ve 1,3,5 tri-terbutilbenzen (TTBB)’in $CO_2$ ile temas ettiği zaman meydana gelen erime noktasındaki düşüş modellemiş, geliştirilen model bu maddelerin erime noktalarındaki düşüşü başarılı bir şekilde hesaplamaktadır.

Anahtar Kelimeler: POSS, Süperkritik Karbondioksit, Faz Davranışı, Çözünürlük, Yarı Deneysel Yoğunluk Temelli Modeller

To My Dearest Grandparents Fatma and Enver Dumanlılar

# ACKNOWLEDGEMENTS

I would like to express my gratitude to my supervisor, Assoc. Prof. Dr. Çerağ Dilek Hacıhabiboğlu for her continuous and invaluable guidance, advice, encouragements, patience and criticism throughout the research.

I am thankful to Prof. Dr. İsmail Tosun for their contribution in activity coefficient calculation. Also, I would like to thank to Prof. Dr. Işık Önal and İlker Tezsevin for their invaluable advice and support in DFT studies.

I would like to thank to Middle East Technical University Scientific Research Projects Coordination Unit for supporting this research under the grant numbers YLT-304-2018-3669 and GAP-304-2018-2660.

I would like to thank to my beloved lab mates Merve Özkutlu Demirel and Yağmur Çulhacıoğlu for their support, suggestions and invaluable friendship. And heartfelt thanks to my friends for their friendships and unforgettable memories during the study: Nur Ber Emerce, Berkan Atman, Soner Yaşar, Merve Sarıyer, Ezgi Gözde, Özge Batır, Özge Şen and Berrak Erkmen. I would also like to thank specially to Dilara Danacı for her invaluable friendship and support since high school years and Ezgi Abacıoğlu for her patience, understanding and precious friendship.

A very special thank you to Mehmet Tabak for his endless and invaluable patience, understanding, support, memories and love during my all METU life.

Above all, although this is not enough to define my feelings, I would like to express my greatest thank to my dear mom and dear dad; Halide Dumanlılar and Özcan Dumanlılar for their endless love and encouragement, through whole my life no matter what happens. Also, I owe my grandfather and grandmother: Fatma Dumanlılar and Enver Dumanlılar a great depth of gratitude for growing me with great and endless love.

# TABLE OF CONTENTS

CHAPTERS

# LIST OF TABLES

TABLES

# LIST OF FIGURES

FIGURES

# LIST OF ABBREVIATIONS

| ABBREVIATIONS | |
|---|---|
| AADT | Absolute Average Deviation of Melting Temperature |
| AARD% | Average Absolute Relative Deviation Percentage |
| CMG | Calculation Model Combining with Excess Gibbs |
| C-W | Chrastil Modified by Wang Model |
| d-A | Del Valle and Aguilera Model |
| DSC | Differential Scanning Calorimetry |
| EOS | Equation of State |
| K-J | Kumar and Johnston Model |
| LCVM | Linear Combination of the Huron-Vidal and Michelsen |
| MIBPOSS | Methacrylisobutyl POSS |
| MIOPOSS | Methacrylisooctyl POSS |
| MST | Mendez-Santiago and Teja Model |
| MTD | Melting Temperature Depression |
| NIST | National Institute of Standards and Technology |
| P$_L$LA | Poly($_L$-lactic acid) |
| PMMA | Poly(methyl methacrylate) |
| POSS | Polyhedral Oligomeric Silsesquioxanes |
| RESS | Rapid Expansion of a Supercritical Solution |
| SAS | Supercritical Anti Solvent |

| | |
|---|---|
| SCF | Supercritical Fluid |
| SMS | Semi-predictive Model using Solubility |
| TFPOSS | Trifluoropropyl POSS |
| TGA | Thermogravimetric Analysis |
| TTBB | 1, 3, 5-tri-terbutylbenzene |
| UNIFAC | UNIversal Functional Activity Coefficient |

## LIST OF SYMBOLS

SYMBOLS

| | |
|---|---|
| $[A]$ | Solute concentration, |
| $[AB]$ | Concentration of the solvato complex |
| a, b, c, d | Constant parameters of density based models |
| $a_{mn}$ | UNIFAC group interaction parameter between group n and m |
| $[B]$ | Solvent concentration |
| $b_{mn}$ | UNIFAC group interaction parameter between group n and m |
| $f_{OC}^{S}$ | Fugacity of pure organic component at solid phase |
| $f_{OC}^{L}$ | Fugacity of pure organic component at solid phase |
| $\widehat{f_{OC}^{L}}$ | Fugacity of the organic compound in the mixture at liquid phase |
| $\Delta H$ | Total reaction heat |
| $\Delta H_{fus}$ | Solid-solid transition enthalpy |
| $\Delta H_{solv}$ | Heat of solvation |
| $\Delta H_{vap}$ | Heat of vaporization |
| k | Association number |
| $K_{eq}$ | Equilibrium constant |
| $MW_A$ | Molecular weight of solute $[A]$ |
| $MW_B$ | Molecular weight of solvent $[B]$ |
| N | Number of experiments |
| $P$ | Pressure |
| $P_c$ | Critical pressure |
| $P_{ref}$ | Reference Pressure |

| | |
|---|---|
| $Q$ | Group surface parameter |
| $q$, $q_s$, $q_v$ | Constants |
| $q_i$ | Molecular surface area of component i |
| R | Group volume parameter of component i |
| $r_i$ | Molecular volume |
| S | Mass concentration of the solute |
| $scCO_2$ | Supercritical carbon dioxide |
| T | Temperature |
| $T_c$ | Critical temperature |
| $T_{nm}$ | Normal melting temperature |
| $T_t$ | Temperature at triple point |
| $\Delta T\%$ | Relative average percent deviations of melting temperature |
| $\lvert\Delta T\%\rvert$ | Absolute average percent deviations of melting temperature |
| $\vartheta_{OC}^{L}$ | Molar liquid volume |
| $\vartheta_{OC}^{S}$ | Molar solid volume |
| $\Delta\vartheta_{fus}$ | Molar volume change during fusion |
| X | Mole fraction of group m |
| $x_{OC}$ | Mole fraction of pure organic compound |
| $y_i^p$ | Calculated solubility mole fraction |
| $y_i^e$ | Experimental solubility mole fraction |

GREEK SYMBOLS

| | |
|---|---|
| $\gamma_i$ | Activity coefficient of component i |
| $\gamma_i^C$ | Combinatorial activity coefficient of component i |
| $\gamma_i^R$ | Residual activity coefficient of component i |
| $\phi_i$ | Volume fraction of component i |
| $\theta_i$ | Surface area fraction of component i |

| | |
|---|---|
| $\upsilon_k^{(i)}$ | Number of subgroup k in component i |
| $\mathit{\Gamma}_k$ | Contribution of functional group k in component i |
| $\Theta_m$ | Area fraction of group m |
| $\psi_{nm}$ | Group interaction parameter between group n and m |
| $\rho$ | Solvent density |
| $\rho_{ref}$ | Reference density |

# CHAPTER 1

# INTRODUCTION

## 1.1. Polyhedral Oligomeric Silsesquioxane (POSS)

Silsesquioxanes are silicon-based materials that have different molecular structures such as random, ladder, cage, and partial-cage structure, shown in Figure 1.1 [1]. In recent years, silsesquioxanes with cage-like structures, named as Polyhedral Oligomeric Silsesquioxanes (POSS), have become attractive materials due to their hybrid structures [2,3]. These nano-cage structures are composed of an inorganic silica-oxygen frame and adjustable organic (R) groups, which are attached to each silica atom [1-5].

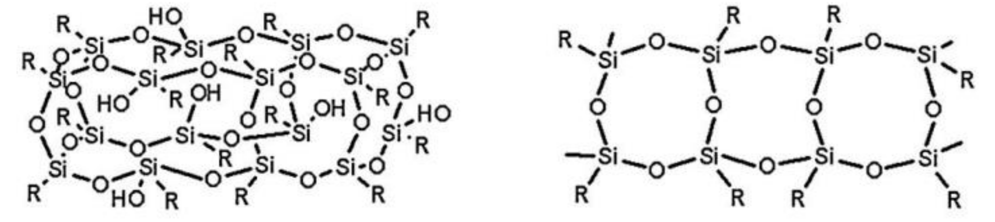

**(a)**
**(Random structure)**

**(b)**
**(Ladder structure)**

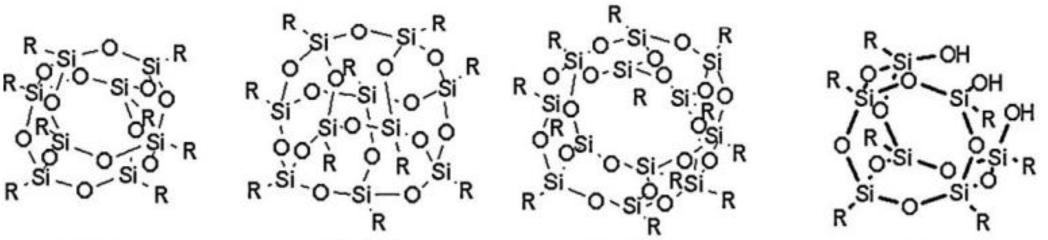

**(c) T8** **(d) T10** **(e) T12** **(f)**

**(Cage structures)** **(Partial cage structure)**

*Figure 1.1.* Different structures of silsesquioxane molecules (a) random structure; (b) ladder structure; (c), (d), (e) cage structure based on number of silica atom; (d) partial cage structure [1]

Their general chemical formula is $(RSiO_{1.5})_n$, where n equals to eight, ten, or twelve and R represents hydrogen or groups such as alkyl, alkene, acrylate, aryl arylene, amine, or hydroxyl [1,2,4-8]. There is a plethora of application fields of POSS due to their versatility. Mainly, they have been used as nanofillers into polymer [6,9,10] to improve flame retardancy, oxidation resistance, thermal stability, and mechanical properties of the polymer [11-14]. Compared to the traditional nanofillers such as clays, carbon fiber, and carbon nanotube, advantages of POSS include smaller molecular size, lower density, and particularly its availability to chemical modification [7, 9]. Organic groups (R) of POSS generally improve its compatibility with polymer and allow it to be efficiently dispersed in the polymeric matrix [1,7,9,11]. POSS are also preferred in medical applications such as dental nanocomposites [15], tissue engineering [16,17], cancer drug delivery application [18] and cardiovascular applications [19] due to their biocompatibility in addition to their chemical and thermal stability. The other novel researches of POSS have been carried out on optics and electrical systems such as organic light emitting diodes technology [20,21] and nanosensor technology [22].

### 1.2. Supercritical Fluids (SCF)

The temperature-pressure diagram of pure substances with the supercritical region is given in Figure 1.2 [23]. The critical point, which is the highest temperature and pressure point where the gas and liquid phase of the substances coexist, is shown as a black dot in the figure. Materials with the temperature and pressure above critical point are defined as supercritical fluid (SCF), as shown in the figure.

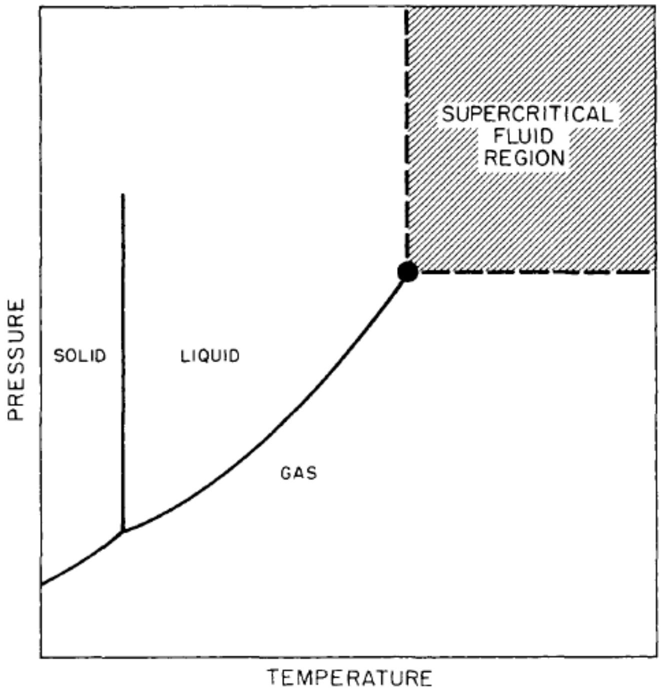

*Figure 1.2.* Temperature-pressure diagram [23]

SCFs show an intermediate behavior between the liquid and gas phase. They have both gas like transport properties such as viscosity, diffusivity and surface tension, and liquid like density. In the SCF region, the small change of temperature or pressure causes significant variations of all these thermophysical properties due to their sensitivity to temperature and pressure [24,25]. For instance, a slight increase in pressure at constant temperature causes increasing of SCF density [26]. On the other hand, at the same condition, viscosity increases while diffusivity decreases. These tunable thermophysical properties also allow improvement of SCF solvent characteristics because the density is proportional to solvent power [23], whereas the viscosity and diffusivity are related to mass transfer. These properties make SCFs a convenient alternative to traditional fluids for industrial applications such as extraction processes, particle formation, or polymer processing [24,27]. The physical properties of the gas (G), liquid (L) and SCF are compared in Table 1.1 [26]. There are many SCFs at different critical temperature ($T_c$) and pressure ($P_c$) but most widely used one is supercritical carbon dioxide ($scCO_2$).

Table 1.1. *The physical properties of liquid, gas and SCF phases [26]*

| **Phase** | **Density (g/mL)** | **Viscosity (cp)** | **Diffusivity ($cm^2/s\times10^3$)** |
|---|---|---|---|
| G | 0.001 | 0.5-3.5 | 10-1000 |
| L | 0.8-1 | 30-240 | 0.005-0.02 |
| SCF | 0.2-0.9 | 2-10 | 0.01-0.3 |

### 1.2.1. Supercritical Carbon Dioxide ($ScCO_2$)

Supercritical carbon dioxide ($scCO_2$) is a widely applied green solvent because it is non-flammable, abundant, low-cost, and nontoxic, and it decreases the use of organic solvents [27]. Besides, it has a lower critical temperature (31.1 °C) and pressure (7.4 MPa) than many other fluids [23]; therefore, supercritical processes of $CO_2$ generally require relatively lower equipment and operation cost compared to those using other solvents. The lower critical temperature of $CO_2$ also allows the processing of heat sensitive materials without thermal degradation.

$CO_2$ has a non-polar chemical structure so molecules which are non-polar and have low molecular weight dissolve in $scCO_2$ [28]. However, some polar molecules containing groups such as carbonyl, hydroxide or fluorine [29] can also dissolve in $scCO_2$ because of the quadrupole moment of $CO_2$, which allows it to exhibit both Lewis acid and Lewis base nature, thus specific interactions with polar molecules [28,30]. However, most of the high molecular weight polar molecules are insoluble in $scCO_2$ so cosolvent can be added to the system to increase the solubility of the molecules in $scCO_2$ [29].

All of these properties of $scCO_2$ allow it to be used in many applications. To illustrate, it is used for the extraction, processing, and preservation of fruit and vegetables [31]. Its another application is particle formation, such as the formation of titanium dioxide spherical particles [32]. Additionally, it can be used for drying and cleaning purposes [29], supercritical fluid chromatography applications [27], coating processes [29] and polymer applications [33, 34].

### 1.2.2. Phase behavior in $ScCO_2$

The phase behavior and solubility knowledge of materials, especially novel materials, in $scCO_2$ have critical importance to design or improve environmentally benign $scCO_2$ processes. Depending on the desired design, materials with different levels of solubility can be used. For instance, Rapid Expansion of a Supercritical Solution (RESS) processes requires soluble materials in $scCO_2$, while it needs to be almost insoluble materials in $scCO_2$ for Supercritical Anti-Solvent (SAS) processes [35].

Solubility is expressed as the maximum amount of material, or solute, dissolved in SCF solvent under a certain temperature and pressure to form homogeneous SCF solution for SCF systems. In brief, it is the mole or weight fraction of the solute in the SCF solution under equilibrium [36,37]. The solubility in SCF is influenced by solutes and solvent features such as their molecular structure and polarity, solvent density and solute vapor pressure besides operating temperature and pressure effects [35,38].

As mentioned in section 1.2, solvent density, related to solvent power, is tunable with temperature and pressure [23]. The temperature and pressure impact the solubility differently from each other. For instance, the solubility of any solids in $scCO_2$ decreases with decreasing solvent density due to a reduction in the pressure [36,39]. On the other hand, the solubility relationship with temperature is more complicated than pressure because the variation of the temperature impacts not only solvent density but also solute vapor pressure [40]. The solubility of solids in $scCO_2$ depends on whether increasing solvent density or decreasing solute vapor pressure with the decreasing temperature is more dominant or not. Generally, in low pressure region, solvent density is more dominant than solute vapor pressure due to the higher compressibility, so the solubility increases due to increasing solvent density with the decreasing temperature. However, in high pressure region, the solubility increases due to increasing the vapor pressure with increasing temperature since the solute vapor pressure effect on the solubility is more dominant.

When crystalline solids are brought in contact with a compressed fluid, which is in most cases carbon dioxide, melting point depression (MTD) of the solid is observed due to increasing pressure [23, 41]. Melting temperature depression phenomena is affected by solubility and hydrostatic pressure effects. As shown in Figure 1.3 [42], which represents the melting temperature depression experimental data of naphthalene and biphenyl in dense $CO_2$, the behavior of melting temperature ($T_m$) has different trends for different ranges of pressure. At the low pressure region, when pressure is increased, $T_m$ decreases due to the solubility of the compressed $CO_2$, in the molten crystal solid [43-45]. However, the melting temperature behavior changes suddenly at the high pressure region. In this region, the solubility effect is overcome by the hydrostatic pressure effect, so $T_m$ starts to increase [43-45].

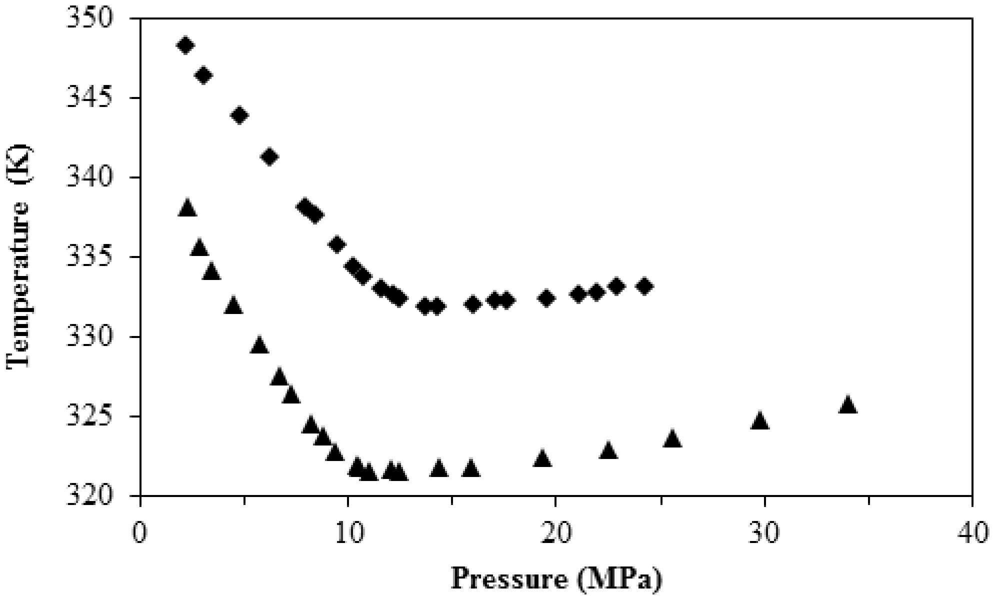

*Figure 1.3.* Melting temperatures of crystalline solids in the presence of compressed $CO_2$; naphthalene ( ◆ ), biphenyl ( ▲ ) (adapted from [42])

## 1.3. Solubility Modelling in ScCO$_2$

The information about the solubility of solutes in scCO$_2$ is fundamental to develop any scCO$_2$ application or process. However, there are limited data about the solubility of solutes in literature, and the experimental determination of solubility can be very time consuming and expensive [46,47]. To circumvent these problems, theoretical models have been improved to predict the solubility of solutes in scCO$_2$. Generally, the solubility of solutes in scCO$_2$ is modeled by two main approaches, which are the “Equation of state (EOS)” or “semi-empirical density based model” [38]. Rather than EOS model, semi-empirical density based model is much preferred due to the lack of knowledge about the features of complex-structured solutes, such as acentric factor, critical temperature, critical pressure, and the solute vapor pressure which are essential parameters to use EOS model [38,48,49]. The available experimental solubility data at different temperature and pressure is used to derive the semi-empirical density-based models which give a relationship between the solvent density and the solubility within the range of temperature and pressure [49]. Six different density based semi-empirical models, the Chrastil model, Del Valle and Aguilera model, Kumar and Johnston model, Bartle model, Mendez-Santiago, and Teja model and Chrastil modified with Wang model, are explained in this section.

### 1.3.1. Chrastil Equation

In 1982, Chrastil derived an equation by fitting the experimental solubility data of some solutes in scCO$_2$ [50] to predict the solubility at any temperature or pressure. This model is one of the oldest and most extensively used semi-empirical density based model, which is based on the equilibrium between the solute and solvent (SCF) [51]. The solution AB$_k$ consists of one mole solute A and k mole solvent B, and they are in equilibrium with each other.

$A + kB \leftrightarrow AB_K$

The equilibrium constant, $K_{eq}$, and the logarithm of it are presented in Eq. 1 and in Eq. 2.

$$K_{eq} = \frac{[AB_k]}{[A][B]^k} \tag{1}$$

$$lnK_{eq} + ln[A] + kln[B] = ln[AB_k] \tag{2}$$

where;

$[A]$ is the solute concentration,

$[B]$ is the solvent concentration,

$[AB]$ is the concentration of the solvato complex

k is an association number.

The expression of $K_{eq}$ can be shown as in Eq. 3. In this equation, $\Delta H_{solv}$ and $q_s$ represent the heat of solvation and a constant, respectively.

$$lnK_{eq} = \frac{\Delta H_{solv}}{RT} + q_s \tag{3}$$

$[A]$ might be defined from the Clausius-Clapeyron equation, as given in Eq. 4.

$$ln[A] = \frac{\Delta Hvap}{RT} + q_v \tag{4}$$

where $\Delta Hvap$ and $q_v$ are the heat of solute vaporization and a constant, respectively.

Eq. 3 and Eq. 4 are substituted into Eq. 2 to obtain in Eq. 5:

$$\frac{\Delta H}{RT} + q + kln[B] = \ln[AB_k] \tag{5}$$

$\Delta H$ and $q$ represent the total reaction heat and a constant, respectively. $\Delta H$ is the sum of the heat of solvation and heat of vaporization while $q$ is the sum of $q_s$ and $q_v$.

Solute and solvent concentrations are stated as in Eq. 6. and Eq. 7.

$$[AB_k] = \frac{S}{MW_A + kMW_B} \tag{6}$$

$$[B] = \frac{\rho}{MW_B} \tag{7}$$

where $MW_A$ and $MW_B$ respectively represent the molecular weight of solute, $[A]$ and molecular weight of solvent $[B]$; $S$ and $\rho$ are the mass concentration of the solute and solvent density, respectively.

Equations 6 and 7 substituted into Eq. 5 to obtain Eq. 8

$$\frac{\Delta H}{RT} + q + kln\rho - klnMW_B = lnS - \ln(MW_A + kMW_B) \tag{8}$$

Eq. 8 is rearranged as

$$S = \rho^k \exp(\frac{a}{T} + b) \tag{9}$$

k is related to the number of the molecules in the solvate complex, and a is associated with the heats of solvation and vaporization of the solute, while b is directly related to the molecular weights of the solute and the solvent. They are defined as Equations 10 and 11.

$$a = \frac{\Delta H}{R} \tag{10}$$

$$b = \ln(MW_A + kMW_B) + q - klnMW_B \tag{11}$$

In order to compare the models, the mass concentration of the solute, S, can be defined as Eq. 12 with considering the mole fraction of solute, $y_2$.

$$S = \frac{y_2 \rho Mw_{solute}}{Mw_{SCF}(1-y_2)} \tag{12}$$

### 1.3.2. Del Valle and Aguilera Equation

The relationship between temperature, density, and solubility which is given in the Chrastil equation, had been improved over the following years by Del Valle and Aguilera to predict the solubility vegetable oil in compressed $CO_2$ taking into account the variation in the solute’s heat of vaporization with temperature [52]. Thus, Del Valle and Aguilera (d-A) equation took the form of Eq. 13.

$$S = \rho^k \exp(\frac{a}{T} + b + \frac{c}{T^2}) \tag{13}$$

The adjustable parameters k, a and b in d-A model given in Eq. 13 are the same with the Chrastil model.

### 1.3.3. Kumar and Johnston Equation

Kumar and Johnson [53] model proposes a linear relationship between $lny_2$, which is the natural logarithm of solvent mole fr., and $\rho$, as given in Eq. 14. The adjustable parameter "a" is associated with the total enthalpy change as the summation of the enthalpy of vaporization and enthalpy of solvation [49]. Also, the adjustable parameter "k" is similar with that of Chrastil Equation.

$$lny_2 = k\rho + \frac{a}{T} + b \tag{14}$$

### 1.3.4. Bartle Equation

Bartle [54] developed a solubility model (Eq. 15) which uses a reference pressure ($P_{ref}$), which is 0.1 MPa and a reference density ($\rho_{ref}$) as 700 kg/m$^3$.

$$ln\left(\frac{y_2P}{P_{ref}}\right) = k\left(\rho_1 - \rho_{ref}\right) + \frac{a}{T} + b \tag{15}$$

The parameter "a" is directly associated with the vaporization of the solute ($\Delta H_{vap}$) as given in the following equation. "k" value is similar with Kumar and Johnston Equation.

$$\Delta H_{vap} = -Ra \tag{16}$$

### 1.3.5. Mendez-Santigo and Teja Equation

The Mendez-Santigo&Teja proposed a model incorporating the Antoine equation for the solute sublimation pressure due to lack of the sublimation pressure data of most of the solutes [55].

$$T\ln(y_2P) = b + k\rho + aT \tag{17}$$

### 1.3.6. Chrastil Modified by Wang Equation

This semi-empirical density-based model was modified from the Chrastil equation by Wang [49]. This modified equation is given in Eq. 18.

$$\ln(S_j) = b + \frac{f}{T} + e\,\rho_1 + d\ln(P) \tag{18}$$

In this equation adjustable parameter "b" is related to the entropy of solvation and the vapor pressure of the solute, while "f" is relevant to the enthalpy of solvation, the molar volume and the vapor pressure of the solute. The parameter "e" is associated with the second virial coefficient of the solute ($B_{22}$), the mixed second virial coefficient ($B_{12}$), the molar volume, and the association number ($k$), while the last adjustable parameter "d" is equal to ($k$-1).

## 1.4. Melting Temperature Depression Modelling in ScCO$_2$

In order to model melting temperature depression, solid-liquid phase equilibrium is established by equating the solid phase fugacity of the pure organic compound, $f_{OC}^{S}$, to the liquid phase fugacity of the organic compound in the liquid mixture of the organic compound and CO$_2$, $\widehat{f_{OC}^{L}}$, as given in Eq. 19 [56].

$$f_{OC}^{S}(\mathrm{T},\mathrm{P}) = \widehat{f_{OC}^{L}}(T,P) \tag{19}$$

$\widehat{f_{OC}^{L}}(T,P)$ can be expressed as Eq. 20.

$$\widehat{f_{OC}^{L}}(T,P) = f_{OC}^{L}(T,P) \cdot \gamma_{OC} \cdot x_{OC} \tag{20}$$

In this equation, $f_{OC}^{L}(T,P)$, $\gamma_{OC}$ and $x_{OC}$ represent the liquid phase fugacity, activity coefficient, and mole fraction of the pure organic compound in liquid phase, respectively.

Equations 19 and 20 can be used to obtain Eq. 21

$$\ln(\gamma_{OC} x_{OC}) = -ln\left(\frac{f_{OC}^{L}(T,P)}{f_{OC}^{S}(T,P)}\right) \tag{21}$$

Pressure effect is considered to model the melting point depression, so $f_{OC}^{L}(T,P)$ and $f_{OC}^{S}(T,P)$ are expressed as equations 22 and 23.

$$f_{OC}^{L}(T,P) = f_{OC}^{L}(T,P_0) \cdot exp\left(\frac{\vartheta_{OC}^{L} \cdot (P-P_0)}{RT}\right) \tag{22}$$

$$f_{OC}^{S}(T,P) = f_{OC}^{S}(T,P_0) \cdot exp\left(\frac{\vartheta_{OC}^{S} \cdot (P-P_0)}{RT}\right) \tag{23}$$

Eq. 22 and Eq. 23 are substituted to Eq. 21 to obtain Eq. 24.

$$\ln(\gamma_{OC}x_{OC}) = -\left[ln\left(\frac{f_{OC}^{L}(T,P_0)}{f_{OC}^{S}(T,P_0)}\right) + \frac{(\vartheta_{OC}^{L}-\vartheta_{OC}^{S}) \cdot (P-P_0)}{RT}\right] \tag{24}$$

$\vartheta_{OC}^{L}$ and $\vartheta_{OC}^{S}$ are the molar liquid volume and molar solid volume of the solute, respectively. $(\vartheta_{OC}^{L} - \vartheta_{OC}^{S})$ can be expressed as $\Delta\vartheta_{fus}$, which is molar volume change during fusion.

The term of $\frac{f_{OC}^{L}(T,P_0)}{f_{OC}^{S}(T,P_0)}$, given in Eq. 25, was derived by Prausnitz et al., [57] by making three assumptions. First, the triple point temperature ($T_t$) is almost equal to the normal melting temperature ($T_{nm}$) so, $T_t$ is replaced with $T_{nm}$. Second, solid-solid transition enthalpy is eliminated because fusion enthalpy ($\Delta H_{fus}$) is very large compared to solid-solid transition enthalpy. The last assumption is that the change of heat capacity between the liquid and solid phase is negligible [57].

$$ln\left(\frac{f_{OC}^{L}(T,P_0)}{f_{OC}^{S}(T,P_0)}\right) = \frac{\Delta H_{fus}}{R}\left(\frac{1}{T} - \frac{1}{T_{nm}}\right) \tag{25}$$

Eq. 25 is combined with Eq. 24 to obtain Eq. 26.

$$\ln(\gamma_{OC}x_{OC}) = \frac{\Delta H_{fus}}{R}\left(\frac{1}{T_{nm}} - \frac{1}{T}\right) - \frac{\Delta\vartheta_{fus}\,(P-P_0)}{RT} \tag{26}$$

where, $P$, $P_0$, $T$, and $R$ represent the system pressure, atmospheric pressure $P_0$, which is taken as 0.1 MPa, the melting temperature under the pressurized gas and gas constant, respectively.

In Eq. 26, $\Delta\vartheta_{fus}\ (P - P_0)$ term represents the hydrostatic pressure effect, while $\ln(\gamma_{OC}x_{OC})$ represents the solubility effect. Hydrostatic pressure effect always rises melting temperature since $\Delta v_{fus}$ is always positive during the melting [58].

### 1.4.1. Determination of Activity Coefficient

There are many theoretical approaches to calculate activity coefficient, $\gamma_{OC}$, such as empirical models, local composition model, and group contribution models. When experimental data are not available, group contribution models are the best choice due to their dependency on the molecular structure [59,60]. In group contribution methods, it is assumed that the system consists of functional groups instead of molecules [61,62]. This is presented in Figure 1.4. This brings in the advantage of group contribution methods since there is less number of functional groups than the possible number of molecules [63]. UNIversal Functional Activity Coefficient (UNIFAC) is one of the group contribution models, which was developed by Fredenslund et al. [64]. UNIFAC is the most used and successful group contribution method because of its accurate predictions [63].

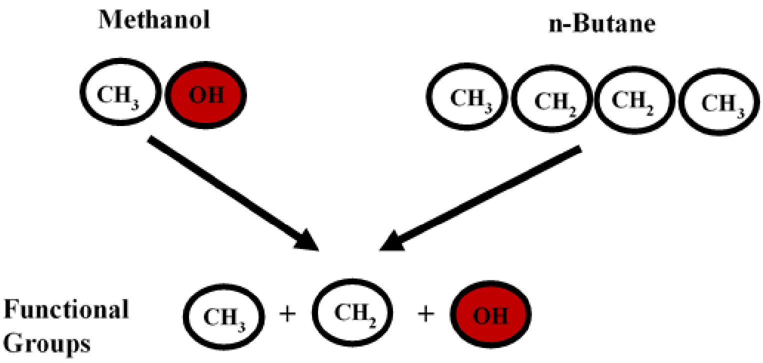

*Figure 1.4.* Functional groups for methanol and n-butane (adapted from [63])

In the UNIFAC model, the activity coefficient is calculated by using Eq. 27. As it can be seen in Eq. 27, the activity coefficient comprises of "combinatorial activity coefficient", $\gamma_i^C$, and "residual activity coefficient", $\gamma_i^R$. The parameter $\gamma_i^C$ considers the size and shape of molecules in the mixture while $\gamma_i^R$ takes into account enthalpic energy interactions [63,65]. After determining groups and subgroups, the procedure [60,65,66] is followed in order to calculate both combinatorial activity coefficient, $\gamma_i^C$, and residual activity coefficient, $\gamma_i^R$.

$$ln\,\gamma_i = ln\,\gamma_i^C + ln\,\gamma_i^R \tag{27}$$

$ln\,\gamma_i^C$ takes into account the surface area and volume of each molecule, and is calculated by

$$ln\,\gamma_i^C = ln\left(\frac{\phi_i}{x_i}\right) + 5\,q_i\,ln\left(\frac{\theta_i}{\phi_i}\right) + l_i - \frac{\phi_i}{x_i}\sum_j x_j\,l_j \tag{28}$$

where the volume fraction, $\phi_i$, and the surface area fraction, $\theta_i$ are defined as

$$\phi_i = \frac{r_i\,x_i}{\sum_j r_j\,x_j}\ ,\qquad \theta_i = \frac{q_i\,x_i}{\sum_j q_j\,x_j}\ ,\qquad l_i = 1 - r_i + 5\,(r_i - q_i). \tag{29}$$

In Eq. 29 the molecular volume, $r_i$ , and the surface area, $q_i$, are determined from

$$r_i = \sum_k \upsilon_k^{(i)}\,R_k,\qquad q_i = \sum_k \upsilon_k^{(i)}\,Q_k \tag{30}$$

where R and Q are the group volume and the surface parameters, respectively; $\upsilon_k^{(i)}$ represents the number of subgroup k in component i.

$\gamma_i^R$ is dependent on intermolecular forces of groups and it is calculated as

$$ln\,\gamma_i^R = \sum_k \upsilon_k^{(i)}\left[ln\,\Gamma_k - ln\,\Gamma_k^{(i)}\right]. \tag{31}$$

Contribution of functional group k, $\Gamma_k$, and contribution of functional group k, $\Gamma_k^{(i)}$, are determined as

$$ln\,\Gamma_k\left(or\,ln\,\Gamma_k^{(i)}\right) = Q_k\left[1 - ln(\sum_m \Theta_m\,\psi_{mk}) - \sum_m \frac{\Theta_m\,\psi_{km}}{\sum_n \Theta_n\,\psi_{nm}}\right] \tag{32}$$

where the area fraction of group m, $\Theta_m$, mole fraction of group m in the mixture, $X_m$, and group interaction parameter, $\psi_{mn}$, are defined as

$$\Theta_m = \frac{Q_m X_m}{\sum_n Q_n X_n}, \qquad X_m = \frac{\sum_j v_m^{(j)} x_j}{\sum_j \sum_n v_m^{(j)} x_j} \tag{33}$$

$$\psi_{mn} = exp\left(-\frac{a_{mn}}{T}\right). \tag{34}$$

Although the UNIFAC model predicts reliable results, it shows weakness to predict asymmetric systems' activity coefficient [61,63,67]. The reason for this weakness in the UNIFAC model is that interaction parameters between two main groups are calculated as temperature independent, like as Eq. 34 [61]. To solve this problem, different models were developed such as "modified Huron–Vidal second order" (MHV2), "linear combination of the Huron-Vidal and Michelsen" (LCVM) and "predictive Soave–Redlich–Kwong" (PSRK) [67]. Among all of these models, LCVM is chosen in this study because researches show that LCVM performs better prediction than other models for high pressure, and asymmetric systems [67,68]. According to LCVM rule, the interaction parameter, $\psi_{mn}$, is calculated as Eq. 35.

$$\psi_{mn} = exp\left(-\frac{a_{mn}+b_{mn}\,(T-298.15)}{T}\right) \tag{35}$$

### 1.5. Aim of the Study

This study focuses on the phase equilibria of novel $CO_2$ philic molecules and $CO_2$ binary systems. Under this focus, there are three objectives of this study. One of them is to investigate the solubility of POSS molecules in $scCO_2$ with molecular structures in which one of the functional groups attached to the cage Si atoms is different from the others to see the effects of two different functional groups on the $CO_2$-affinity of POSS molecules. Up to date, the common property of all the studied POSS molecules is that the functional groups attached to the Si atom were identical. Therefore, under this scope, the phase behavior studies of methacrylisobutyl (MIBPOSS) which has seven isobutyl groups and a methacryl group and methacrylisooctyl (MIOPOSS) which has seven isooctyl groups and a methacryl group (MIOPOSS) in $scCO_2$ have been carried out and their phase behaviors have been compared with their previously studied counterparts which have single functional groups such as methacryl POSS [5], isobutyl POSS [5], and isooctyl POSS [5]. The temperature and pressure of the phase behavior experiments were selected based on some requirements of the supercritical fluid technologies such as lower operating cost and safety. The other important reason of this selection was to compare our solubility results with those of the previously studied POSS. This would contribute to the production of knowledge on the "molecular structure-sc$CO_2$ affinity" relationships of these molecules, which can be used for tailoring novel materials that can be more advantageous for supercritical $CO_2$ technologies.

The second aim of the study is to model the solubility data of MIBPOSS and MIOPOSS in sc$CO_2$ by using the semi-empirical density based model. Thus, in the lack of the experimental data, the solubility of the POSS in sc$CO_2$ could be determined by interpolation or extrapolation using these equations.

The last objective is to model the melting point depression of three aromatic components which are naphthalene, biphenyl and 1,3,5-tri-tert-butylbenzene (TTBB) in sc$CO_2$ so the melting temperature behavior of these aromatic components could be estimated by using the model in case of lack of experimental data. In order to develop this model, UNIFAC group contribution method with LCVM mixing rule was used to estimate the activity coefficients.

# CHAPTER 2

# LITERATURE SURVEY

## 2.1. Solubility of POSS in $ScCO_2$

Recently, many investigations have been performed on the phase behavior of novel materials in $scO_2$ to design or improve processes of these materials with $scCO_2$. In 2013, Dilek [69] conducted a study about phase behavior of POSS, functionalized with a fluoroalkyl group, in $scCO_2$. The solubility of trifluoropropyl POSS (TFPOSS) in $scCO_2$ was measured at 8.3–14.8 MPa pressure and 308–323 K temperature ranges by observing the cloud point of the POSS. The maximum solubility was determined as $1.7\times10^{-3}$ mole fr. at these pressure and temperature ranges. Isobaric temperature increment decreases the solvent density while increasing solute vapor pressure. The solubility of TFPOSS in $scCO_2$ decreases with isobaric temperature increment since the negative effect of solvent density is more dominant than the positive effect of solute vapor pressure. The solubility data were used to determine optimum processing conditions for high-pressure surface modification of a poly(methyl methacrylate) (PMMA) sheet. As a result of the analysis of processed PMMA sheets, it was observed that the POSS coated the PMMA uniformly by processing the sheets with the POSS-$CO_2$ solution.

Kanya and Dilek [5] investigated the solubility of various POSS with different functional groups such as octamethyl, methacryl, isooctyl, and octaisobutyl at 308 K and 323 K. The results showed that once POSS is modified with specific functional groups, it can be solubilized in $scCO_2$. For example, octamethyl POSS was insoluble in $scCO_2$, while the rest of the selected POSS types were soluble in $scCO_2$. It was found that solubility of methacryl and isooctyl POSS in $scCO_2$ increases with isobaric decrease in the temperature; also, the solubility of isooctyl POSS is greater than the solubility of methacryl POSS. On the other hand, crossover pressure was observed for the system of octaisobutyl POSS and $scCO_2$. When the system pressure of octaisobutyl POSS-$scCO_2$ is below the crossover pressure, the solubility decreases with an increase in the temperature due to the adverse effect of the solvent density on the solubility. In the opposite case, a positive contribution of solute vapor pressure is dominant, so solubility of octaisobutyl POSS increases with increasing the temperature.

Demirtaş and Dilek [70] studied the solubility of POSS, which has alkylsiloxy functional group. The solubility of octatrimethylsiloxy POSS in $scCO_2$ was performed at the pressure and temperature ranges of 8-13 MPa 308-328 K. It was found that that solubility of siloxy POSS in $scCO_2$ is up to $8.3\times10^{-3}$ mole fr. The results showed that among all the studied functionalized POSS types, octatrimethylsiloxy POSS exhibits the greatest affinity to $CO_2$, and highest solubility at the studied conditions due to the rotational flexibility of the siloxane groups and low cohesive energy density, thus weak solute-solute interactions compared to the other functionalized POSS. The solubility of the POSS in $scCO_2$ increases with isothermal pressure increment, while it decreases with isobaric temperature increment due to the contribution of $CO_2$ density. In this study, six different density based semi-empirical models were applied for correlating the experimental solubility of the POSS in $scCO_2$. Absolute average relative deviations (AARD) of the models were minimized and found as in the range of 22–25%.

## 2.2. Application of POSS-$ScCO_2$ Systems

$CO_2$-philic POSS can be used in various supercritical $CO_2$ applications. In the study of Eris et al. [71], the solubility knowledge of TFPOSS in $scCO_2$ was applied to develop an optofluidic use. In this study, U-shaped fibers were formed by filling the molds with TFPOSS. Then, the fibers were embedded in the silica solution and allowed to gelation and aging. $ScCO_2$ was preferred to extract TFPOSS and dry the wet gel because the POSS was known to be soluble in $scCO_2$ [69]. Thus, the U-shaped hollow channel in the gel was created by this extraction. The channel was filled with water after making aerogel surface hydrophobic by the reaction of the silanol groups at the surface with hexamethyldisilazane in the existence of $scCO_2$. In the study, curved shaped optofluidic waveguides were obtained. Additionally, improved waveguiding by coupling light into the water-filled channel and monitoring the channel output were observed.

Costeux and Zhu [72] developed nanofoam formation by processing thermoplastic polymer with $scCO_2$ for thermal insulation. Polymethyl methacrylate and styrene acrylonitrile copolymers were combined with $CO_2$-philic nanoparticle, such as methacryl POSS, and processed with $scCO_2$, thus cell nucleation density of the polymers was improved three orders of magnitude.

Novendra and coworkers [73], studied on porous film formation of highly crystalline poly($_L$-lactic acid) ($P_LLA$) at different conditions. In this study, the solvent casting method was used to form $P_LLA$ composites with a $CO_2$-philic additive and a non $CO_2$-philic additive. Then, the $P_LLA$ composites and $P_LLA$ without any additive were processed with $scCO_2$ to obtain porous polymeric films. The results showed that processed $P_LLA$ without any additive does not provide porous polymeric films while $CO_2$-philic TFPOSS (10 % by weight)-$P_LLA$ composite provides homogenous pore formation in the polymeric film at the same processing conditions. When the amount of TFPOSS was increased to 30 % by weight at the same processing conditions, the pore formation is more homogenous and raises compared to 10 % TFPOSS - $P_LLA$ composite. On the other hand, octamethyl POSS (non $CO_2$-philic)-$P_LLA$ composites did not provide pore formation under the same processing conditions.

## 2.3. Melting Temperature Depression in $ScCO_2$

Knowledge about melting temperature depression is as essential as solubility knowledge in order to develop and design $scCO_2$ processes. Thus, many investigations were performed to determine melting temperature depression of different materials such as aromatic compounds [42,74], polymers [41,75,76] and ionic liquids [77,78,79] in $scCO_2$. One of these studies was performed for naphthalene and biphenyl by Cheong and coworkers [42]. The solid-liquid-vapor equilibrium curve of the compounds in $scCO_2$ was constructed by observing the "first freezing point method". They investigated that melting temperatures of the aromatic compounds were depressed by dense $CO_2$ by up to 331.95 K at 14.36 MPa for naphthalene and 321.61 K at 11.02 MPa for biphenyl. Then, the liquid concentrations of these compounds were correlated by using the approach of Prausnitz [57].

Takebayashi et al. [58] carried out the experimental and theoretical investigation of melting temperature depression of naphthalene and biphenyl in $scCO_2$. They modeled solid-vapor and solid-liquid phase equilibria using Peng Robinson EOS with van der Waals mixing rule and analyzed effects of the hydrostatic pressure and the solubility on melting temperature depression. Results showed that the hydrostatic pressure effect increases the melting temperature up to 7 ˚C and 9 ˚C for naphthalene and biphenyl, respectively. On the other hand, solubility effect decreases melting temperature about 34 ˚C at 20 MPa for both aromatic compounds.

Hong and coworkers [80] modeled solid-liquid-vapor equilibria of nine different compounds in $scCO_2$ by using two different approaches, which are "Semi-predictive model using solubility (SMS)" and "calculation model combining with excess Gibbs (CMG)", in order to predict melting temperature of the compounds, depressed by $CO_2$, and solute solubility in $CO_2$. For the SMS model, the interaction parameter, $k_{12,}$ was predicted by using Peng Robinson EOS with van der Waals mixing rule to correlate solute solubility in $CO_2$. Then, solid-liquid equilibrium was calculated by implementing fugacity calculation from EOS or activity coefficient calculation from UNIFAC model to predict melting temperature. For CMG model, Peng Robinson EOS was used with different mixing rules such as LCVM, modified-LCVM and MHV1(modified Huron–Vidal first order), mixing rule. The results indicated that the

SMS model and CMG with mLCVM give acceptable results for the prediction of melting temperature of compound and solute solubility in $scCO_2$ and liquid.

Dilek and coworkers [74] studied the phase behavior of an aromatic compound with tertiary butyl groups, which is 1,3,5-tri-tert-butylbenzene (TTBB), in $scCO_2$. TTBB is solid at ambient temperature with a melting temperature of 343 K and is highly soluble in $scCO_2$. The results of the study exhibited that TTBB exhibits a melting point depression when it is in contact with dense $CO_2$ and a decrease of 45 K in its melting temperature is observed at a pressure of 3.11 MPa. However, the pressure-induced melting depression behavior of this system was not modelled.

# CHAPTER 3

# EXPERIMENTAL METHOD

## 3.1. Solubility Experiments

### 3.1.1. Materials

Methacrylisobutyl POSS (MIBPOSS) (%99 purity, Hybridplastics, Hattiesburg, MS, USA) is a white powder solid with a molecular weight of 943.64 g/mol, and bulk density of 0.613 g/cm$^3$. Methacrylisooctyl POSS (MIOPOSS) (%99.4 purity, Hybridplastics, Hattiesburg, MS, USA) is a viscous liquid with a viscosity of 4036 cP, molecular weight of 1336.38 g/mol and density of 0.995 g/cm$^3$. They have the same molecular formula, $(RSiO1.5)_n$ with n=8, but R represent i-butyl for solid POSS and i-octyl for liquid POSS as shown in Figure 3.1. Both chemicals were used without further purification. Carbon dioxide (99.9%) was supplied from Linde Gas (Ankara, Turkey).

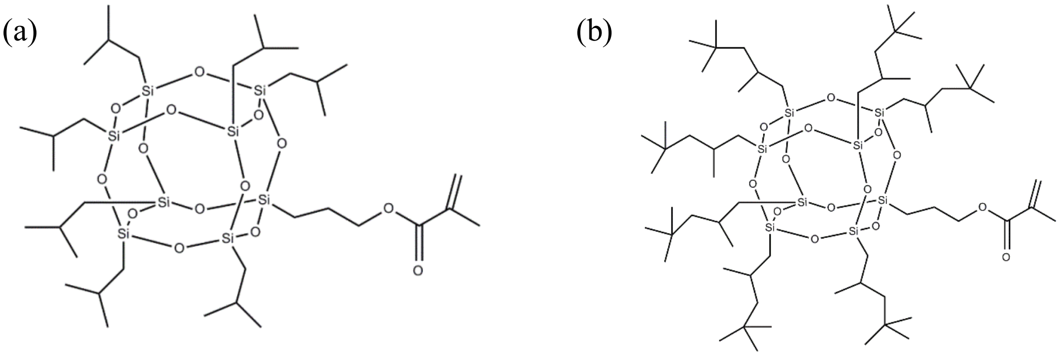

*Figure 3.1.* Chemical structures of (a) methacrylisobutyl POSS, (b) methacrylisooctyl POSS

### 3.1.1. Experimental Set-up

The phase behavior experiments were carried out by using a high-pressure set-up consisting of a high-pressure syringe pump (Teledyne ISCO-260D), a custom-made, stainless-steel, jacketed high-pressure vessel coupled with a thermocouple (Omega Engineering KMQXL-IM150U-150) and a pressure transducer (Omega Engineering PX419), a magnetic stirrer, a $CO_2$ tank, and two water circulators, one used for controlling the pump temperature (VWR, 89202-972) and the other used for the vessel temperature (Polyscience, 9112). The vessel had two sapphire windows, a rupture disc, and two needle valves for inlet and outlet flows, and its inner volume was 30.6 ± 0.05 $cm^3$. The accuracies of thermocouple and a pressure transducer are ± 0.5 K and ± 0.03 MPa, respectively. The experimental set-up is presented in Figure 3.2.

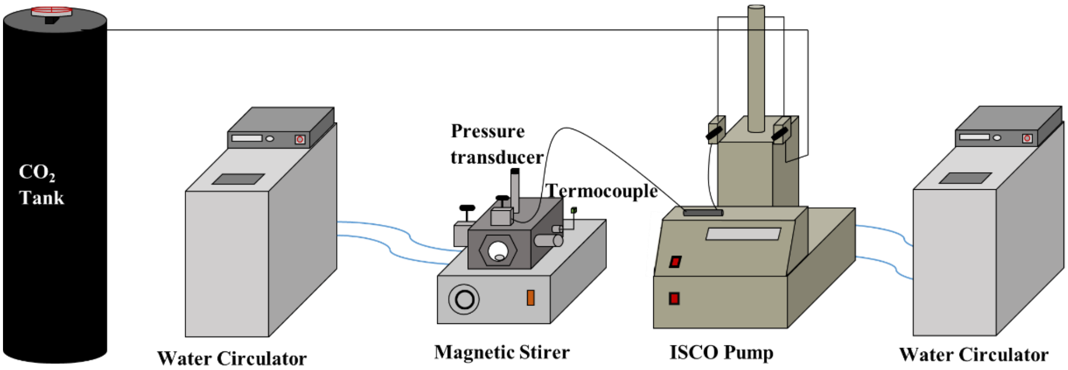

*Figure 3.2.* The experimental *set*-up

### 3.1.2. Cloud and Dew Point Measurement

The solubilities of MIBPOSS and MIOPOSS in $scCO_2$ were determined by dew and cloud point measurements, respectively at 308, 313, 318 and 323 K. The same experimental procedure was applied for the other POSS-$CO_2$ system [5, 69, 70]. First, the amount of POSS was measured with an accuracy of ± 0.0001 g and loaded in the vessel along with a magnetic stirring bar. The vessel was placed on the magnetic stirrer, and the temperature of the vessel was arranged to the desired value using the water circulator connected to the vessel jacket. Next, the vessel was connected to the syringe pump, which was working at constant pressure mode. The pump's temperature was kept constant at 298 K using the water circulator connected to the pump jacket and pressure of the syringe pump was set as the desired pressure, which was high enough to dissolve all POSS in $scCO_2$. Prior to the loading of the vessel with $CO_2$, the line between the vessel and the syringe pump was filled, and the volume of $CO_2$ in the pump reservoir was recorded. The inlet valve was opened slowly by keeping the vessel temperature constant, and the vessel was loaded with $CO_2$ until the pressure of the vessel was equal to syringe pump pressure. Next, the volume of $CO_2$ in the pump reservoir was recorded. After the loading process, the leakage test was performed. In order to calculate the amount of $CO_2$ loaded into the cell, the volume difference between initial and final recorded volume of $CO_2$ in the pump reservoir and $CO_2$ density data at 298 K and the setting syringe pump pressure, obtained from NIST (National Institute of Standards and Technology) Chemical WebBook [81], were used. Both weight fraction and mole fraction of POSS and $CO_2$ were determined from the weight of the $CO_2$ and POSS loaded to the vessel. Once the POSS-$CO_2$ system becomes homogenous and single phase, the line was connected to the exit valve and $CO_2$ was depressurized at constant temperature slowly (almost 0.007 MPa/s). When the POSS phase separated from the single-phase solution, visually detectable cloudiness was formed. This point was cloud or dew point depending on the state of the separated phase, so pressure at this point was recorded. Next, the cell was completely depressurized and cleaned with the proper solvent. This procedure was applied for both MIBPOSS and MIOPOSS at 308, 313, 318, and 323 K. Three experiments were selected randomly at each temperature and were carried out on different days following the same experimental procedure. The highest standard deviation of the cloud point pressures was ± 0.19 MPa for MIBPOSS, while it was found to be ± 0.28 MPa for the dew point pressures of MIOPOSS.

## 3.2. Melting Point Depression Experiments

In the phase behavior studies of the MIBPOSS-$CO_2$ binary system, the liquid formation was observed indicating the melting point depression of MIBPOSS. The following procedure was followed for determining the melting pressures of MIBPOSS at 308, 313, 318 and 323 K. To determine the melting pressure, the same experimental set up, given in Figure 3.2, was used. First, MIBPOSS was loaded to the vessel at a desired value. Then the vessel was sealed and connected to the syringe pump, while the temperature of the vessel was increased to the set temperature using the water circulator connected to the vessel jacket. Next, the line between the vessel and ISCO pump was loaded with $CO_2$ while the vessel inlet valve was closed. Then the inlet valve of the vessel was opened, and $CO_2$ was loaded very slowly, at about a rate of 0.007 MPa/s. When melting was observed, the pressure was recorded as melting point pressure. This procedure was repeated three times for 308, 313, 318 and 323 K.

## 3.3. Differential Scanning Calorimetry (DSC)

The thermal behavior of the studied solid POSS, which is MIBPOSS, was performed by Shimadzu DSC-60 analyzer under the nitrogen atmosphere. For this analysis, MIBPOSS was heated from room temperature to 300 ˚C with 10 ˚C /min temperature rate and 50 mL/min nitrogen flow rate. Then, melting temperature and heat of fusion of MIBPOSS were determined by using the DSC thermogram.

## 3.4. Thermal Gravimetric Analysis (TGA)

The weight changes of MIBPOSS and MIOPOSS with increasing temperature were determined by using Shimadzu DTG–60H thermal gravimetric analysis device. These analyses were carried out under nitrogen atmosphere with 50 mL/min nitrogen flow rate. Both MIBPOSS and MIOPOSS were heated from room temperature to 800 ˚C. Thus decomposition temperature and behavior of the POSS were observed.

# CHAPTER 4

# THEORETICAL METHOD

## 4.1. Solubility Modelling

Chrastil model, Del Valle and Aguilera model, Kumar and Johnston model, Bartle model, Mendez-Santiago and Teja model and Chrastil modified with Wang model were used to correlate the solubility data of MIBPOSS and MIOPOSS. The accuracy between the calculated and experimental solubility of the POSS in $scCO_2$ was obtained by using absolute average relative deviation (AARD), which is expressed as Eq. 36 where $y_i^p$ is calculated solubility mole fraction, $y_i^e$ is experimental solubility mole fraction and N is the number of experiments. The empirical parameters of the models were obtained by minimizing the AARD by using the MATLAB simulation program.

$$AARD\ (\%) = \frac{1}{N}\sum_i^N \left( \left| \frac{y_i^e - y_i^p}{y_i^e} \right| \right) \cdot 100 \tag{36}$$

## 4.2. Melting Point Depression Modelling

The melting temperature depressions of aromatic compounds, including naphthalene, biphenyl, and 1,3,5-tri-tert-butylbenzene (TTBB) with compressed $CO_2$ have been modeled by constructing the solid-liquid phase equilibrium of the compounds in $scCO_2$. The equilibrium equation was given in Eq. 26 and explained in the introduction section.

$$\ln(\gamma_{OC} x_{OC}) = \frac{\Delta H_{fus}}{R}\left(\frac{1}{T_{nm}} - \frac{1}{T}\right) - \frac{\Delta\vartheta_{fus}\,(P-P_0)}{RT} \tag{26}$$

Fusion enthalpies, molar volume changes upon the fusion and normal melting temperature data of naphthalene, biphenyl, and TTBB are presented in Table 4.1. For naphthalene and biphenyl, these data were available in the literature; but there was no data of molar volume change upon the fusion of TTBB. Thus, the solid molar volume of TTBB was determined by using helium pycnometer. On the other hand, in order to measure the liquid molar volume of TTBB, a certain amount of the material was heated up to its melting temperature, and the liquid molar volume of it was determined by using a graduated cylinder.

Table 4.1. *Physical properties of naphthalene, biphenyl and TTBB*

| | $T_{nm}$(K) | $\Delta H_{fus}\left(\frac{kj}{mol}\right)$ | $\vartheta_{OC}^{S}\left(\frac{cm^3}{mol}\right)$ | $\vartheta_{OC}^{L}\left(\frac{cm^3}{mol}\right)$ | $\Delta\vartheta_{fus}\left(\frac{cm^3}{mol}\right)$ |
|---|---|---|---|---|---|
| Naphthalene | 353.45 [58] | 19.31[58] | 111.9 [58] | 131.2[58] | 19.3[58] |
| Biphenyl | 342.65[58] | 18.58[58] | 131.0 [58] | 155.8 [58] | 24.8 [58] |
| TTBB | 343.00 [74] | 11.92 [82] | 272.3 | 289.1 | 16.8 |

Pressure and liquid mole fraction data of the naphthalene and biphenyl were obtained from Cheong et al. [42], while they were obtained from Dilek et al. [74] for TTBB.

In order to calculate the activity coefficient of the organic compound, $\gamma_{OC}$, by using the UNIFAC group contribution method, groups and subgroups of the naphthalene, biphenyl and TTBB were determined from their molecular structures, given in Figure 4.1. The details of these determinations are presented in the appendix.

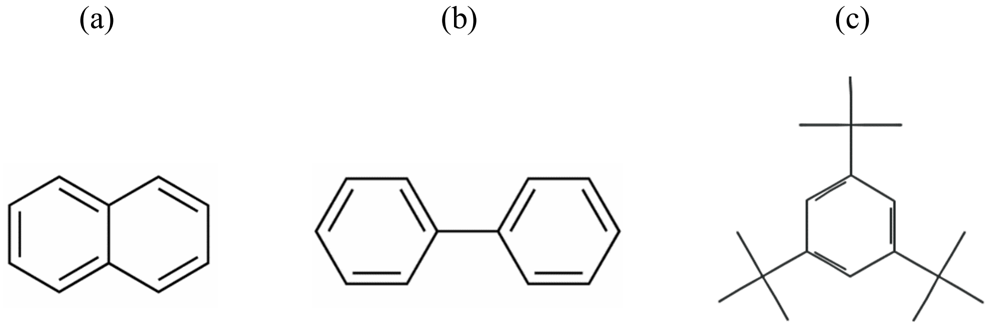

*Figure 4.1.* Molecular structures of (a) naphthalene, (b) biphenyl and (c) TTBB

The group volume ($R_k$) and surface area ($Q_k$) parameters of subgroups are obtained from literature and given in Table 4.2. Also, interaction parameters between each group are given in Table 4.3.

Table 4.2. *Surface Area ($Q_k$) and group volume ($R_k$) parameters for the UNIFAC model [80,83-85]*

| **Group** | **Subgroup** | **$R_k$** | **$Q_k$** |
|---|---|---|---|
| $CH_2$ | $CH_3$ | 0.9011 | 0.848 |
| | $CH_2$ | 0.6744 | 0.540 |
| | CH | 0.4469 | 0.228 |
| | C | 0.2195 | 0.000 |
| ACH | ACH | 0.5313 | 0.400 |
| | AC | 0.3652 | 0.120 |
| $CO_2$ | $CO_2$ | 1.296 | 1.261 |

Table 4.3. *Group interaction parameters for the LCVM mixing rule [80,83,85]*

| **Group k** | **Group m** | **$a_{km}$ (K)** | **$a_{mk}$ (K)** | **$b_{km}$** | **$b_{mk}$** |
|---|---|---|---|---|---|
| $CH_2$ | $CH_2$ | 0.00 | 0.00 | 0.00 | 0.00 |
| $CH_2$ | ACH | 61.13 | -11.12 | 0.00 | 0.00 |
| $CH_2$ | $CO_2$ | 116.70 | 110.6 | -0.9106 | 0.5003 |
| ACH | ACH | 0.00 | 0.00 | 0.00 | 0.00 |
| ACH | $CO_2$ | 187.00 | -26.80 | 1.0982 | -1.2348 |
| $CO_2$ | $CO_2$ | 0.00 | 0.00 | 0.00 | 0.00 |

After determining the groups and subgroups, $\gamma_{OC}$ was calculated for each compound from the explained procedure in the introduction section, based on the estimated temperature. Thus, the left-hand side and right-hand side of the Eq. 26 were separately calculated, and whether they were equal or not was checked. Next, iteration of the melting temperature was continued until the right-hand side equals to the left-hand side. These calculations were performed by using Mathcad 15.

# CHAPTER 5

# RESULTS AND DISCUSSION

## 5.1. Phase Behavior of Methacrylisobutyl POSS and Methacrylisooctyl POSS in $scCO_2$

Until today, the effects of different functional groups of POSS on their solubility in $scCO_2$ have been examined with POSS molecules which have a single type of functional groups attached to the Si atoms of the POSS cage [5,69,70]. Within the scope of these studies, solubility experiments of POSS which have fluoroalkyl [69], alkylsiloxy [70], methacrylate [5], isobutyl [5], and isooctyl [5] functional groups, in $scCO_2$ have been carried out at a temperature range of 308 K to 323 K. As a result of these studies, it was observed that the modification of POSS with different functional groups affected their solubility in $scCO_2$ significantly, resulting in a wide variation of solubility, which becomes negligible when POSS is modified with certain functional groups such as methyl or phenyl. Among all the studied functionalized POSS types, POSS with alkylsiloxy groups exhibits the greatest affinity to $CO_2$, and highest solubility at the studied conditions. The highest solubility of octatrimethylsiloxy POSS was measured as $8.3\times10^{-3}$ mole fr. at a $CO_2$ density of 0.59 g/cm$^3$ at 13.36 MPa and 328 K [70].

Recently, we have started to investigate the solubility of POSS molecules in $scCO_2$, where one of the functional groups attached to the cage Si atoms was replaced with a different type. Both types of these groups provide solubility in $scCO_2$ when they are attached to the POSS molecules as a single type of functional group. In this work, two types of POSS molecules have been studied with the explained structure. One of them, a solid POSS has seven isobutyl groups and a methacryl group (MIBPOSS) and the other, a liquid POSS has seven isooctyl groups and a methacryl group (MIOPOSS).

### 5.1.1. Melting Point Depression of Methacrylisobutyl POSS in $scCO_2$

During the solubility experiments of MIBPOSS, pressure-induced melting point depression was observed. This phenomenon is observed for various compounds including aromatic compounds such as naphthalene, biphenyl and 1,3,5-tritertiary butyl benzene [42,74], ionic liquids [77,78,79] and various polymers [41,75,76]. The normal melting temperature of MIBPOSS is found to be 385 K by using the DSC analysis, the thermogram of which is given in Appendix B. The melting temperature of the POSS reduces to 328 K at 4.38 MPa and to 308 K at 4.81 MPa. The pressure-induced melting temperature depression of MIBPOSS with $CO_2$ is given in Figure 5.1.

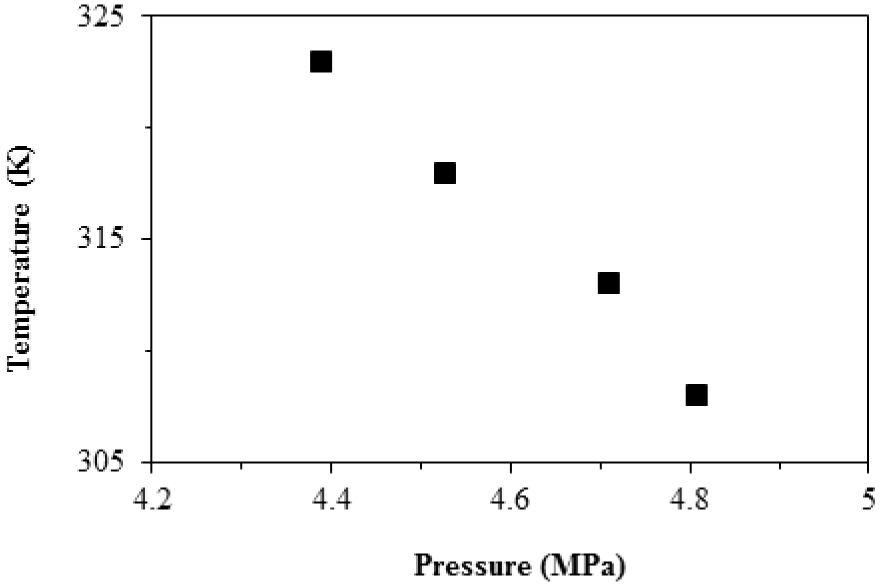

*Figure 5.1.* Temperature vs. pressure graph for MIBPOSS-$CO_2$ binary system ($T_{normal}$=385 K)

### 5.1.2. L-V Equilibria of Methacrylisobutyl POSS-$CO_2$ Binary System

Phase behavior of MIBPOSS in sc$CO_2$ was obtained at a temperature range of 308 K to 323 K with cloud point measurement, explained in experimental section. The solubility data of MIBPOSS in sc$CO_2$ are presented in Table 5.1.

Table 5.1. *The cloud point pressures of MIBPOSS-$CO_2$ binary systems at 308 K, 313 K, 318K and 323 K, and the corresponding carbon dioxide densities.*

| **MIBPOSS weight fraction** | **MIBPOSS mol fraction** | **$P_{cloud}$ (MPa)** | **$CO_2$ Density ($g/cm^3$)** |
|---|---|---|---|
| **308 K** | | | |
| 0.0205 | 0.0010 | 9.00 | 0.6625 |
| 0.0409 | 0.0020 | 10.00 | 0.7130 |
| 0.0598 | 0.0030 | 10.79 | 0.7383 |
| 0.0772 | 0.0039 | 11.27 | 0.7509 |
| 0.0949 | 0.0049 | 12.05 | 0.7680 |
| 0.1101 | 0.0057 | 12.66 | 0.7797 |
| **Repeated Experiments** | | | |
| 0.0205 | 0.0010 | 8.94 | 0.6574 |
| 0.0203 | 0.0010 | 8.96 | 0.6594 |
| 0.0402 | 0.0019 | 10.03 | 0.7137 |
| 0.0401 | 0.0019 | 10.03 | 0.7140 |
| 0.0954 | 0.0049 | 12.38 | 0.7746 |
| 0.0941 | 0.0048 | 12.36 | 0.7742 |
| **313 K** | | | |
| 0.0214 | 0.0010 | 10.43 | 0.6561 |
| 0.0423 | 0.0021 | 11.53 | 0.7031 |
| 0.0605 | 0.0030 | 12.23 | 0.7242 |
| 0.0789 | 0.0040 | 12.92 | 0.7413 |
| 0.0962 | 0.0049 | 13.37 | 0.7510 |
| 0.1143 | 0.0060 | 14.01 | 0.7635 |
| **Repeated Experiments** | | | |
| 0.0214 | 0.0010 | 10.44 | 0.6568 |
| 0.0215 | 0.0010 | 10.45 | 0.6576 |
| 0.0423 | 0.0021 | 11.38 | 0.6979 |
| 0.0426 | 0.0021 | 11.38 | 0.6979 |
| 0.0605 | 0.0030 | 12.38 | 0.7280 |
| 0.0600 | 0.0030 | 12.34 | 0.7271 |

Table 5.1. *(continued)*

| MIBPOSS weight fraction | MIBPOSS mol fraction | $P_{cloud}$ (MPa) | $CO_2$ Density ($g/cm^3$) |
|---|---|---|---|
| **318 K** | | | |
| 0.0230 | 0.0011 | 11.76 | 0.6471 |
| 0.0434 | 0.0021 | 13.01 | 0.6940 |
| 0.0614 | 0.0030 | 13.62 | 0.7112 |
| 0.0829 | 0.0042 | 14.27 | 0.7266 |
| 0.1002 | 0.0052 | 14.64 | 0.7347 |
| 0.1172 | 0.0062 | 15.16 | 0.7450 |
| **Repeated Experiments** | | | |
| 0.0438 | 0.0021 | 13.02 | 0.6942 |
| 0.0444 | 0.0022 | 12.94 | 0.6916 |
| 0.0613 | 0.0030 | 13.76 | 0.7145 |
| 0.0615 | 0.0030 | 13.75 | 0.7143 |
| 0.0805 | 0.0041 | 14.45 | 0.7306 |
| 0.0817 | 0.0041 | 14.29 | 0.7272 |
| **323 K** | | | |
| 0.0245 | 0.0012 | 12.9833 | 0.6354 |
| 0.0441 | 0.0021 | 14.3347 | 0.6821 |
| 0.0627 | 0.0031 | 14.7622 | 0.6937 |
| 0.0819 | 0.0041 | 15.4793 | 0.7110 |
| 0.1004 | 0.0052 | 16.2653 | 0.7274 |
| 0.1185 | 0.0062 | 16.8169 | 0.7376 |
| **Repeated Experiments** | | | |
| 0.0245 | 0.0012 | 12.9074 | 0.6321 |
| 0.0244 | 0.0012 | 13.1005 | 0.6403 |
| 0.0620 | 0.0031 | 15.1001 | 0.7022 |
| 0.0631 | 0.0031 | 15.0932 | 0.7020 |
| 0.1180 | 0.0062 | 16.8928 | 0.7390 |
| 0.1190 | 0.0063 | 16.7066 | 0.7357 |

The binary liquid-vapor equilibrium isotherms of MIBPOSS-$CO_2$ are plotted in Figure 5.2 as mole fractions versus the cloud point pressures (MPa). The binary system remains as a single, homogenous phase indicating complete dissolution at pressures higher than the cloud point pressures, represented by the region on the right hand-side of the isotherms. The solubility of MIBPOSS in $scCO_2$ increases with pressure at isothermal conditions, while it decreases with temperature at isobaric conditions, both of which are due to the variations on the $CO_2$ density. An isothermal pressure increment increases the $CO_2$ density, corresponding to an increase in the solvent power, so the solubility increases. For example, at 308 K, increasing the pressure from about 9 MPa to 13 MPa, an increase in solubility of 4.7 mole % was observed. In this isothermal range, the $CO_2$ density increased from 0.66 to 0.78. An isobaric temperature increment, on the other hand leads to a decrease in the solvent density, and increase in the solute vapor pressure, both of which have opposite effects on the solute solubility in $scCO_2$. The decrease in the solubility of POSS in $scCO_2$ indicates that the negative contribution of density decrease is more dominant than the positive contribution of the solute vapor pressure increase. For example, at about 13 MPa, an isobaric increase in temperature from 308 K to 323 K, leads to a decrease in $CO_2$ density from 0.78 $g/cm^3$ to 0.64 $g/cm^3$, while this decrease dominates the solubility of MIBPOSS in $scCO_2$, which decreases from $5.7\times10^{-3}$ to $1.2\times10^{-3}$.

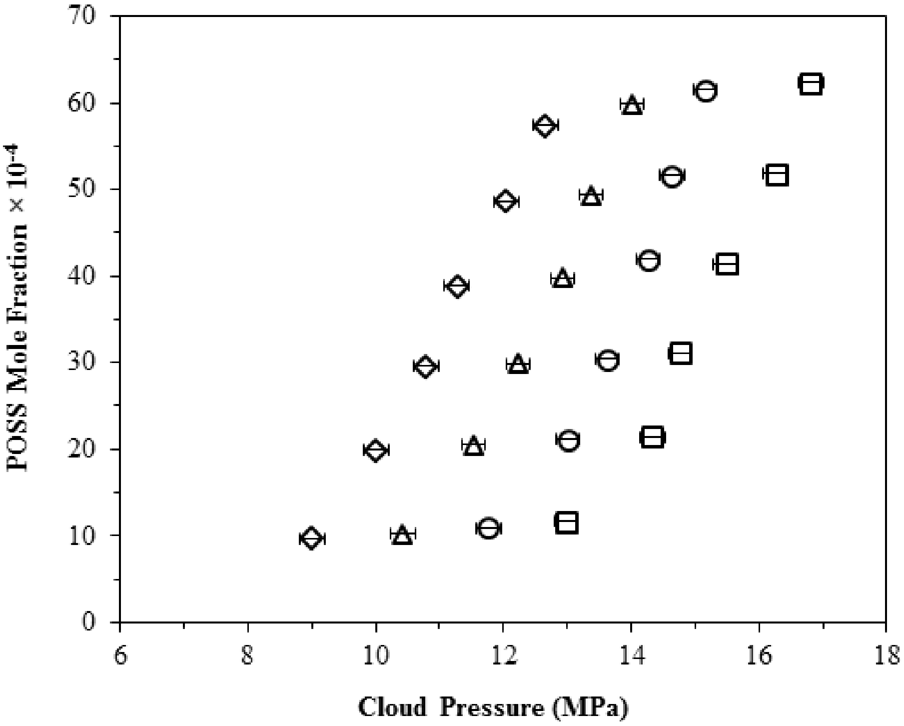

Figure 5.2. *Cloud point isotherms of MIBPOSS at 308 K (◇), 313 K (△), 318 K (○) and 323 K(□) with 0.19 MPa error bars which represent the highest standard deviation of cloud point pressure, calculated from the repeated data.*

Figure 5.3 shows the solubility isotherms of MIBPOSS as mol fr. versus $CO_2$ density at the detected cloud points. At constant $CO_2$ density, the solubility of POSS increases with temperature due to the increase in the chemical potential and thus the vapor pressure of POSS. For instance, at $CO_2$ density of 0.74 g/cm$^3$, an increase in temperature from 308 K to 323 K leads to an increase in the solubility of MIBPOSS in sc$CO_2$ from $3\times10^{-3}$ to $6.2\times10^{-3}$.

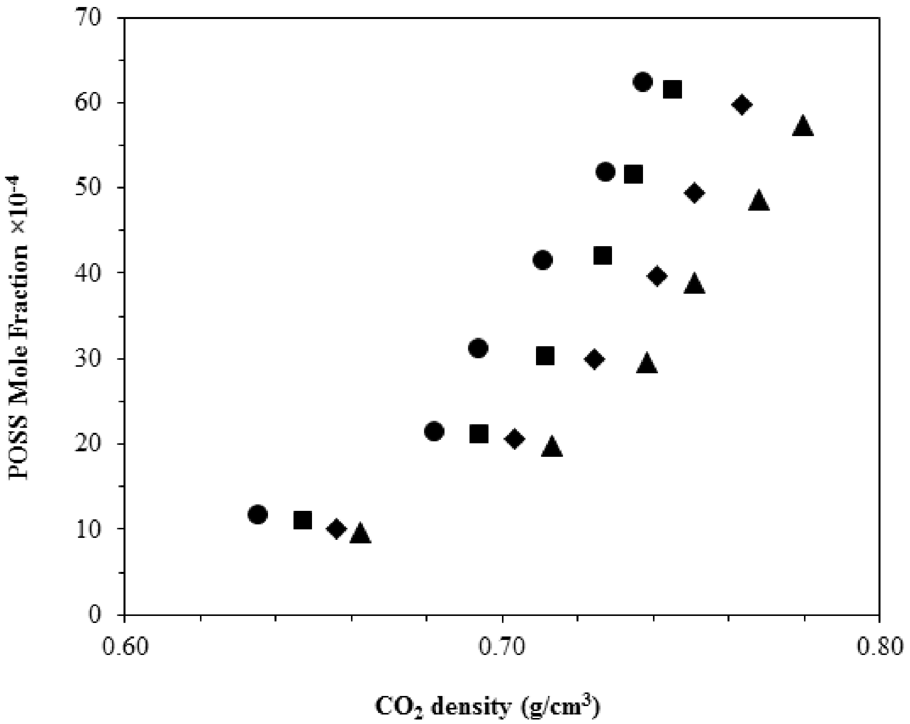

*Figure 5.3.* Solubility (mol fr.) versus $CO_2$ density at the cloud points of MIBPOSS for 308 K (▲), 313 K (◆), 318 K (■) and 323 K (●)

### 5.1.3. L-V Equilibria of Methacrylisooctyl POSS-$CO_2$ Binary System

Phase behavior of MIOPOSS in $scCO_2$ was determined at a temperature range of 308 K to 323 K with dew point measurement. The solubility data of MIOPOSS with dew the dew point pressure and corresponding $CO_2$ are given in Table 5.2.

Table 5.2. *The dew point pressures of MIOPOSS-$CO_2$ binary systems at 308 K, 313 K, 318K and 323 K, and the corresponding carbon dioxide densities.*

| **MIOPOSS weight fraction** | **MIOPOSS mol fraction** | **$P_{dew}$ (MPa)** | **$CO_2$ Density ($g/cm^3$)** |
|---|---|---|---|
| **308 K** | | | |
| 0.0122 | 0.0004 | 12.60 | 0.7786 |
| 0.0196 | 0.0007 | 14.29 | 0.8055 |
| 0.0267 | 0.0009 | 15.33 | 0.8193 |
| 0.0335 | 0.0011 | 16.77 | 0.8357 |
| 0.0407 | 0.0014 | 17.42 | 0.8424 |
| 0.0476 | 0.0016 | 18.54 | 0.8531 |
| **Repeated Experiments** | | | |
| 0.0267 | 0.0009 | 15.35 | 0.8194 |
| 0.0267 | 0.0009 | 15.54 | 0.8218 |
| 0.0335 | 0.0011 | 16.81 | 0.8361 |
| 0.0335 | 0.0011 | 16.86 | 0.8366 |
| 0.0404 | 0.0014 | 17.87 | 0.8468 |
| 0.0403 | 0.0014 | 17.93 | 0.8473 |
| **313 K** | | | |
| 0.0122 | 0.0004 | 14.34 | 0.7694 |
| 0.0198 | 0.0007 | 15.74 | 0.7913 |
| 0.0272 | 0.0009 | 17.13 | 0.8095 |
| 0.0345 | 0.0012 | 17.84 | 0.8177 |
| 0.0413 | 0.0014 | 19.20 | 0.8321 |
| 0.0485 | 0.0017 | 19.42 | 0.8342 |
| **Repeated Experiments** | | | |
| 0.0122 | 0.0004 | 14.23 | 0.7674 |
| 0.0123 | 0.0004 | 14.17 | 0.7663 |
| 0.0272 | 0.0009 | 17.19 | 0.8102 |
| 0.0274 | 0.0009 | 17.16 | 0.8098 |
| 0.0411 | 0.0014 | 19.17 | 0.8318 |
| 0.0413 | 0.0014 | 18.89 | 0.8289 |
| **318 K** | | | |
| 0.0124 | 0.0004 | 15.58 | 0.7528 |
| 0.0208 | 0.0007 | 17.17 | 0.7779 |
| 0.0277 | 0.0009 | 18.27 | 0.7927 |
| 0.0349 | 0.0012 | 19.18 | 0.8036 |
| 0.0422 | 0.0014 | 20.32 | 0.8160 |
| 0.0487 | 0.0017 | 21.15 | 0.8244 |

Table 5.2. *(continued)*

| MIOPOSS weight fraction | MIOPOSS mol fraction | $P_{dew}$ (MPa) | $CO_2$ Density ($g/cm^3$) |
|---|---|---|---|
| **Repeated Experiments** | | | |
| 0.0124 | 0.0004 | 15.76 | 0.7559 |
| 0.0123 | 0.0004 | 15.65 | 0.7540 |
| 0.0350 | 0.0012 | 19.63 | 0.8087 |
| 0.0351 | 0.0012 | 19.50 | 0.8072 |
| 0.0490 | 0.0017 | 21.24 | 0.8252 |
| 0.0496 | 0.0017 | 21.03 | 0.8232 |
| **323 K** | | | |
| 0.0123 | 0.0004 | 16.29 | 0.7279 |
| 0.0194 | 0.0007 | 18.20 | 0.7602 |
| 0.0269 | 0.0009 | 19.82 | 0.7821 |
| 0.0348 | 0.0012 | 20.82 | 0.7939 |
| 0.0424 | 0.0015 | 21.76 | 0.8041 |
| 0.0492 | 0.0017 | 22.06 | 0.8073 |
| **Repeated Experiments** | | | |
| 0.0200 | 0.0007 | 18.03 | 0.7576 |
| 0.0197 | 0.0007 | 18.44 | 0.7637 |
| 0.0272 | 0.0009 | 19.71 | 0.7806 |
| 0.0273 | 0.0009 | 19.92 | 0.7833 |
| 0.0495 | 0.0017 | 22.11 | 0.8077 |
| 0.0494 | 0.0017 | 22.34 | 0.8100 |

The measured dew points of the MIOPOSS-$CO_2$ binary system, representing the liquid-vapor equilibria isotherms at a temperature range of 308 K to 323 K are presented in Figure 5.4. The observations of this binary system are similar to those of MIBPOSS-$CO_2$ binary system, except that for MIOPOSS-$CO_2$ binary system, the dew points along the solubility isotherms occur at higher pressures corresponding to lower solubility mole fractions, indicating that the solubility of MIOPOSS in $scCO_2$ is lower. For example, at 323 K, an increase in pressure form 16 to 22 MPa increases the $CO_2$ density from 0.73 $g/cm^3$ to 0.81 $g/cm^3$. This leads to an increase in solubility of MIOPOSS in $scCO_2$ from $0.4\times10^{-3}$ to $1.7\times10^{-3}$. Also, at about 19 MPa, $CO_2$ density decreases from 0.85 $g/cm^3$ to 0.78 $g/cm^3$ with increasing temperature from 308 K to 323 K. This negative contribution on the solubility dominates the positive contribution of vapor pressure of solute, so the solubility in $scCO_2$ decreases from $1.6\times10^{-3}$ to $0.9\times10^{-3}$.

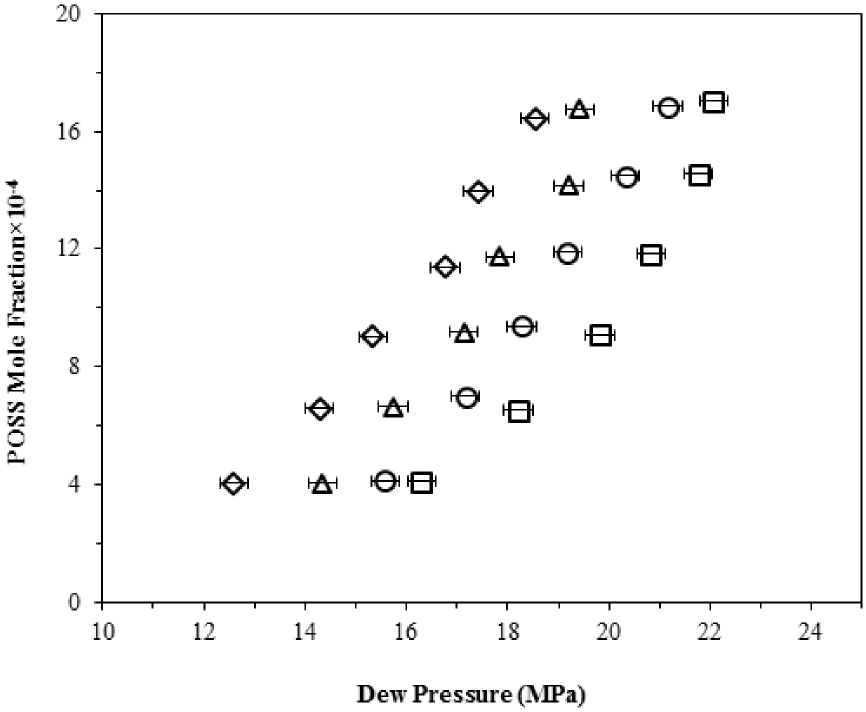

*Figure 5.4.* Dew point isotherms of MIOPOSS at 308 K (◇), 313 K (△), 318 K (○) and 323 K (□) with 0.28 MPa error bars which represent the highest standard deviation of dew point pressure, calculated from the repeated data.

The lower solubility of MIOPOSS in $scCO_2$ with respect to MIBPOSS can also be inferred comparing the solubility versus $CO_2$ density graphs given in Figure 5.3 and Figure 5.5 given for MIBPOSS and MIOPOSS, respectively, which show the solubility (mole fr.) of POSS against the $CO_2$ density. For example, at the $CO_2$ density of 0.78 g/cm$^3$, the solubility of MIBPOSS and MIOPOSS in $scCO_2$ at 308 K are 0.0057 and 0.0004 mol fr., respectively. The higher solubility of MIBPOSS is also observed at 323 K; MIBPOSS solubility, which is 0.0052 mol fr., is greater than that of MIOPOSS, 0.0004 mol fr, at $CO_2$ density of about 0.73 g/cm$^3$. The higher solubility of MIBPOSS is due to the shorter chain length of isobutyl branches of MIBPOSS compared to the isooctyl branches of MIOPOSS. The increased molecular weight due to the increased chain length increases the enthalpic contribution (the absolute value of enthalpy of mixing) and at the same time, decreases the entropy of mixing. Here our results show that increasing molecular weight of POSS by increasing chain length decreases its solubility in $scCO_2$. This shows that the entropic contribution is dominant on the free energy of mixing and solvation of POSS in $scCO_2$ [86]. Regarding to the effect of temperature increase, for MIBPOSS, a 15 K increase in the system temperature from 308 K to 323 K, leads to the highest solubility increase by 0.0032 mol fr., observed at the $CO_2$ density of 0.73 $g/cm^3$. On the other hand for MIOPOSS, the same temperature increment at the $CO_2$ density of 0.81 $g/cm^3$, leads to a 0.001 mol fr. increase in its solubility in $scCO_2$. In the studied pressure and temperature ranges, this shows that the solubility of MIBPOSS is more sensitive to temperature than MIOPOSS, possibly due to the relative increases in the vapor pressures of the solutes with temperature.

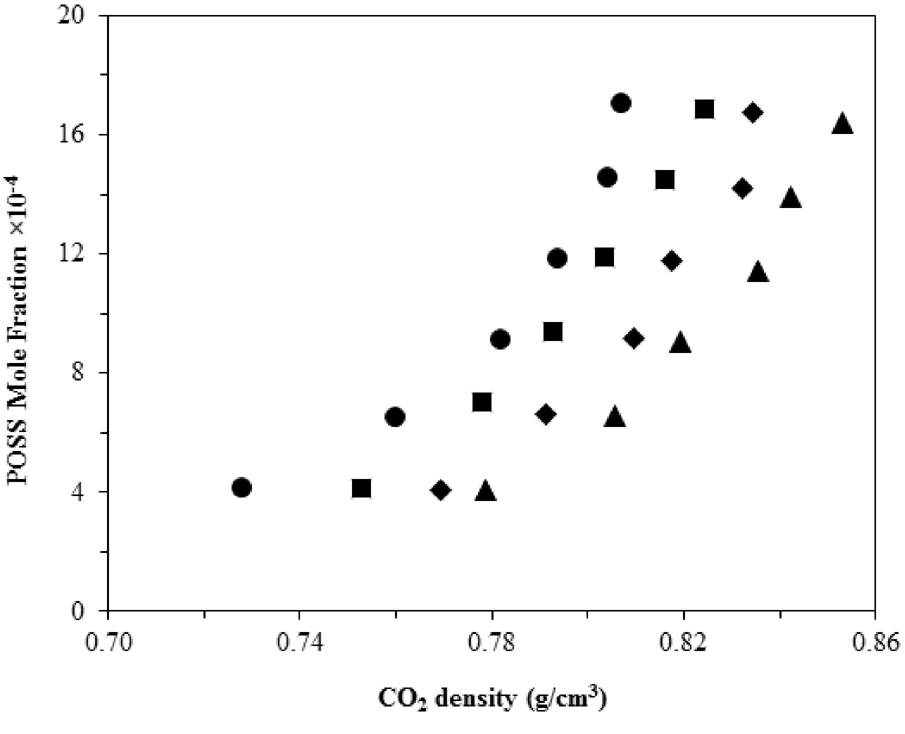

*Figure 5.5.* Solubility (mol fr.) versus $CO_2$ density at the dew points of MIOPOSS for 308 K (▲), 313 K (◆), 318 K (■) and 323 K (●)

## 5.2. Comparison of Methacrylisobutyl POSS-$CO_2$ and Methacrylisooctyl POSS-$CO_2$ Systems with Previous $CO_2$ philic $CO_2$ System Studies

Solubility of MIBPOSS and MIOPOSS in sc$CO_2$ are compared with the previously studied POSS types which contained single type of functional groups of isooctyl, isobutyl or methacryl in order to observe the effect of the changes in the molecular structures of POSS with the replacement of one of the groups attached to the POSS cage [5]. Figure 5.6 shows the solubilities of methacryl POSS, octaisobutyl POSS and isooctyl POSS [5] and MIBPOSS and MIOPOSS in sc$CO_2$ against the $CO_2$ density at cloud or dew points at 308 K (a) and 323 K (b). Among these POSS types with single type of functional groups, methacryl POSS exhibits the lowest solubility in sc$CO_2$, about an order of magnitude lower solubility than its branched-alkyl functionalized counterparts. Therefore, solubilities of MIBPOSS and MIOPOSS in sc$CO_2$ are greater than that of methacryl POSS as expected. However, comparing the solubilities of the branched alkyl chain functionalized POSS with the solubilities of MIOPOSS and MIBPOSS, one may expect that the replacement of one branch of octaisobutyl POSS or one branch of isooctyl POSS with a methacryl group can decrease their solubilities in sc$CO_2$ due to the increasing molecular weight. However, such modifications lead to higher solubility both in cases of MIBPOSS and MIOPOSS, with the prior one exhibiting a greater increase. This increase is attributed to the addition of the carbonyl group enhancing the $CO_2$ philicity of these materials due to specific interactions between the carbonyl group and CO2 such as Lewis acid-base interactions and weak hydrogen bonding interaction [28,86-89]. Addition of the functional groups exhibiting specific interactions with $CO_2$ improves the enthalpy of mixing but at the same time decreases the entropy of mixing as well and increases the cohesive energy density [86]. Therefore, there is an optimum number of CO2-philic functional groups improving the $CO_2$ affinity of the compound up to which enthalpic contribution enhances the solubility of the compound in sc$CO_2$. Above that number, further addition of the functional group decreases the solubility. This is possibly the reason to the more than an order of lower solubility of methacryl POSS in $scCO_2$, compared to MIOPOSS and MIBPOSS.

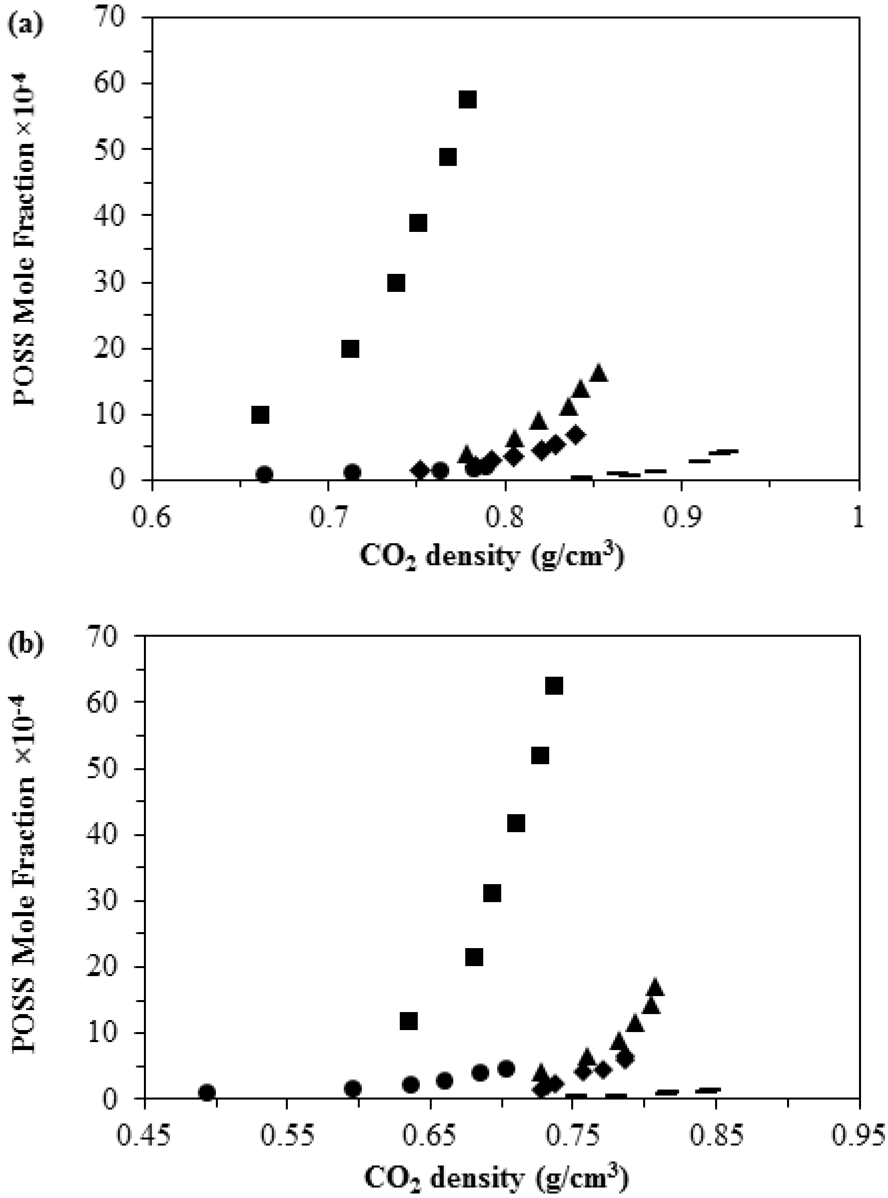

*Figure 5.6.* Solubility (mol fr.) versus $CO_2$ density at the dew points or cloud points of MIBPOSS (■), MIOPOSS (▲), methacryl POSS (–), isooctyl POSS (♦) and octaisobutyl POSS (●) – $CO_2$ binary system (a) 308 K and (b) 323 K

In Figure 5.7, solubilites of MIBPOSS and MIOPOSS in $scCO_2$ are given along with the other $CO_2$-soluble POSS [5,69,70]. Trimethylsiloxy POSS has the highest solubility due to the rotational flexibility of the siloxane groups and low cohesive energy density, thus weak solute-solute interactions compared to the other functionalized POSS [70]. While MIBPOSS exhibits lower solubility in $scCO_2$ than trimethylsiloxy POSS, it exhibited higher solubility than trifluoropropyl POSS although the fluorinated compounds exhibit superior solubility in $scCO_2$.

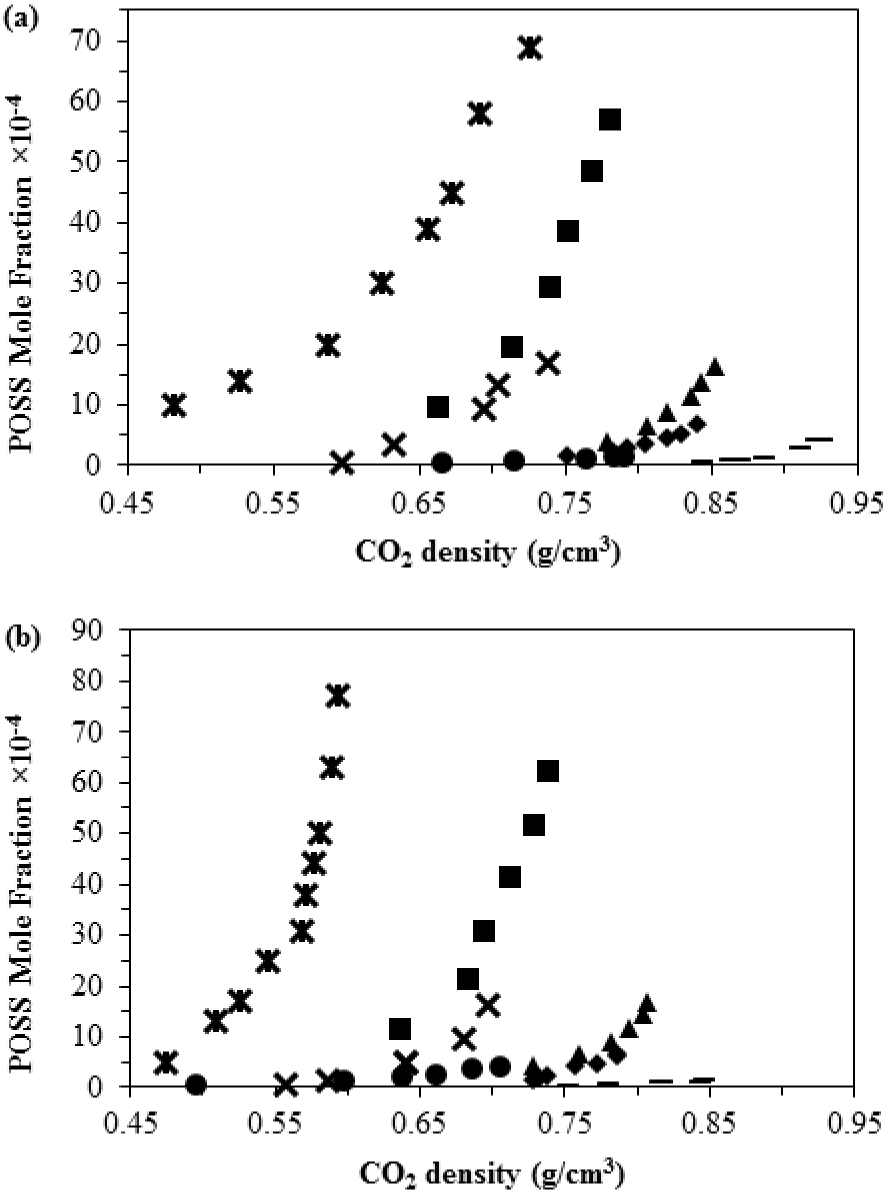

*Figure 5.7.* Solubility (mol fr.) versus CO$_2$ density at the dew points or cloud points of MIBPOSS (■), MIOPOSS (▲), methacryl POSS (–), isooctyl POSS (◆), octaisobutyl POSS (●), trifluropropyl POSS (X), octatrimethylsiloxy POSS (✱), – CO$_2$ binary sytem (a) 308 K and (b) 323 K

## 5.3. Solubility Modelling of Methacrylisobutyl POSS-CO$_2$ and Methacrylisooctyl POSS-CO$_2$ Systems

Solubilities of the MIBPOSS and MIOPOSS in scCO$_2$ were correlated by using six different density based model as summarized in below and these model was applied at the temperature range of 308-323 K. MATLAB was used to find the empirical parameters of the models by minimizing AARD.

$$lnS = b + kln\rho + \frac{a}{T} \qquad \text{(Chrastil)}$$

$$lnS = b + kln\rho + \frac{a}{T} + \frac{c}{T^2} \qquad \text{(d-A)}$$

$$lny_2 = b + k\rho + \frac{a}{T} \qquad \text{(K-J)}$$

$$ln\left(\frac{y_2P}{P_{ref}}\right) = b + k\left(\rho_1 - \rho_{ref}\right) + \frac{a}{T} \qquad \text{(Bartle)}$$

$$T\ln(y_2P) = b + k\rho + aT \qquad \text{(MST)}$$

$$\ln\left(S_j\right) = b + \frac{f}{T} + e\,\rho_1 + d\ln(P) \qquad \text{(C-W)}$$

The calculated solubility of MIBPOSS and MIOPOSS in scCO$_2$ by using the semi-empirical density-based models are given Table 5.3 and 5.4 along with the experimental solubility of the POSS, respectively.

Table 5.3. *The calculated solubility (mol fr.) of MIBPOSS in scCO$_2$*

| **308 K** | | | | | | |
|---|---|---|---|---|---|---|
| **Experimental** | **Chrastil** | **d-A** | **K-J** | **Bartle** | **MST** | **C-W** |
| 0.0010 | 0.0009 | 0.0008 | 0.0009 | 0.0009 | 0.0008 | 0.0009 |
| 0.0020 | 0.0021 | 0.0019 | 0.0020 | 0.0021 | 0.0020 | 0.0020 |
| 0.0030 | 0.0031 | 0.0028 | 0.0030 | 0.0031 | 0.0030 | 0.0030 |
| 0.0039 | 0.0037 | 0.0034 | 0.0037 | 0.0037 | 0.0037 | 0.0036 |
| 0.0049 | 0.0048 | 0.0044 | 0.0049 | 0.0048 | 0.0049 | 0.0049 |
| 0.0057 | 0.0057 | 0.0052 | 0.0059 | 0.0057 | 0.0058 | 0.0059 |

Table 5.3. *(continued)*

| **313 K** | | | | | | |
|---|---|---|---|---|---|---|
| **Experimental** | **Chrastil** | **d-A** | **K-J** | **Bartle** | **MST** | **C-W** |
| 0.0010 | 0.0010 | 0.0010 | 0.0010 | 0.0010 | 0.0010 | 0.0010 |
| 0.0021 | 0.0022 | 0.0021 | 0.0022 | 0.0022 | 0.0022 | 0.0022 |
| 0.0030 | 0.0032 | 0.0030 | 0.0031 | 0.0031 | 0.0030 | 0.0031 |
| 0.0040 | 0.0041 | 0.0039 | 0.0041 | 0.0040 | 0.0040 | 0.0041 |
| 0.0049 | 0.0048 | 0.0046 | 0.0048 | 0.0047 | 0.0047 | 0.0048 |
| 0.0060 | 0.0058 | 0.0055 | 0.0058 | 0.0057 | 0.0057 | 0.0059 |
| **318 K** | | | | | | |
| **Experimental** | **Chrastil** | **d-A** | **K-J** | **Bartle** | **MST** | **C-W** |
| 0.0011 | 0.0011 | 0.0011 | 0.0011 | 0.0011 | 0.0011 | 0.0011 |
| 0.0021 | 0.0025 | 0.0025 | 0.0024 | 0.0024 | 0.0024 | 0.0024 |
| 0.0030 | 0.0033 | 0.0033 | 0.0032 | 0.0032 | 0.0032 | 0.0032 |
| 0.0042 | 0.0042 | 0.0042 | 0.0041 | 0.0041 | 0.0041 | 0.0041 |
| 0.0052 | 0.0047 | 0.0048 | 0.0047 | 0.0046 | 0.0046 | 0.0047 |
| 0.0062 | 0.0055 | 0.0056 | 0.0055 | 0.0055 | 0.0054 | 0.0055 |
| **323 K** | | | | | | |
| **Experimental** | **Chrastil** | **d-A** | **K-J** | **Bartle** | **MST** | **C-W** |
| 0.0012 | 0.0011 | 0.0012 | 0.0012 | 0.0012 | 0.0012 | 0.0012 |
| 0.0021 | 0.0025 | 0.0027 | 0.0025 | 0.0026 | 0.0026 | 0.0025 |
| 0.0031 | 0.0031 | 0.0033 | 0.0030 | 0.0031 | 0.0031 | 0.0030 |
| 0.0041 | 0.0041 | 0.0043 | 0.0040 | 0.0041 | 0.0041 | 0.0040 |
| 0.0052 | 0.0053 | 0.0057 | 0.0053 | 0.0053 | 0.0053 | 0.0053 |
| 0.0062 | 0.0062 | 0.0066 | 0.0062 | 0.0062 | 0.0062 | 0.0062 |

Table 5.4. *The calculated solubility (mol fr.) of MIOPOSS in* *sc*$CO_2$

| **308 K** | | | | | | |
|---|---|---|---|---|---|---|
| **Experimental** | **Chrastil** | **d-A** | **K-J** | **Bartle** | **MST** | **C-W** |
| 0.0004 | 0.0004 | 0.0004 | 0.0004 | 0.0004 | 0.0004 | 0.0004 |
| 0.0007 | 0.0007 | 0.0007 | 0.0007 | 0.0007 | 0.0007 | 0.0007 |
| 0.0009 | 0.0009 | 0.0009 | 0.0009 | 0.0009 | 0.0009 | 0.0009 |
| 0.0011 | 0.0012 | 0.0012 | 0.0012 | 0.0012 | 0.0012 | 0.0012 |
| 0.0014 | 0.0014 | 0.0013 | 0.0013 | 0.0014 | 0.0013 | 0.0013 |
| 0.0016 | 0.0016 | 0.0016 | 0.0016 | 0.0016 | 0.0016 | 0.0016 |
| **313 K** | | | | | | |
| **Experimental** | **Chrastil** | **d-A** | **K-J** | **Bartle** | **MST** | **C-W** |
| 0.0004 | 0.0005 | 0.0004 | 0.0004 | 0.0004 | 0.0004 | 0.0004 |
| 0.0007 | 0.0007 | 0.0007 | 0.0007 | 0.0007 | 0.0007 | 0.0007 |
| 0.0009 | 0.0010 | 0.0010 | 0.0010 | 0.0010 | 0.0009 | 0.0010 |
| 0.0012 | 0.0011 | 0.0011 | 0.0011 | 0.0011 | 0.0011 | 0.0011 |
| 0.0014 | 0.0015 | 0.0015 | 0.0015 | 0.0015 | 0.0015 | 0.0015 |
| 0.0017 | 0.0015 | 0.0015 | 0.0015 | 0.0015 | 0.0015 | 0.0015 |
| **318 K** | | | | | | |
| **Experimental** | **Chrastil** | **d-A** | **K-J** | **Bartle** | **MST** | **C-W** |
| 0.0004 | 0.0005 | 0.0004 | 0.0004 | 0.0004 | 0.0004 | 0.0004 |
| 0.0007 | 0.0007 | 0.0007 | 0.0007 | 0.0007 | 0.0007 | 0.0007 |
| 0.0009 | 0.0010 | 0.0010 | 0.0010 | 0.0010 | 0.0009 | 0.0010 |
| 0.0012 | 0.0011 | 0.0011 | 0.0011 | 0.0011 | 0.0011 | 0.0011 |
| 0.0014 | 0.0015 | 0.0015 | 0.0015 | 0.0015 | 0.0015 | 0.0015 |
| 0.0017 | 0.0015 | 0.0015 | 0.0015 | 0.0015 | 0.0015 | 0.0015 |

Table 5.4. *(continued)*

| **323 K** | | | | | | |
|---|---|---|---|---|---|---|
| **Experimental** | **Chrastil** | **d-A** | **K-J** | **Bartle** | **MST** | **C-W** |
| 0.0004 | 0.0003 | 0.0003 | 0.0004 | 0.0003 | 0.0003 | 0.0004 |
| 0.0007 | 0.0006 | 0.0006 | 0.0006 | 0.0006 | 0.0006 | 0.0006 |
| 0.0009 | 0.0010 | 0.0010 | 0.0010 | 0.0010 | 0.0010 | 0.0010 |
| 0.0012 | 0.0012 | 0.0013 | 0.0012 | 0.0013 | 0.0013 | 0.0012 |
| 0.0015 | 0.0015 | 0.0015 | 0.0015 | 0.0015 | 0.0015 | 0.0015 |
| 0.0017 | 0.0016 | 0.0016 | 0.0016 | 0.0016 | 0.0016 | 0.0016 |

The experimental and calculated solubility data of MIBPOSS and MIOPOSS in $scCO_2$ are plotted against $CO_2$ density at each temperature in Figure 5.8 and 5.9, respectively. The figures show that the models successfully correlate the experimental data of both components and can be used interpolate or extrapolate the solubility values at temperature and pressure closed to studied ones.

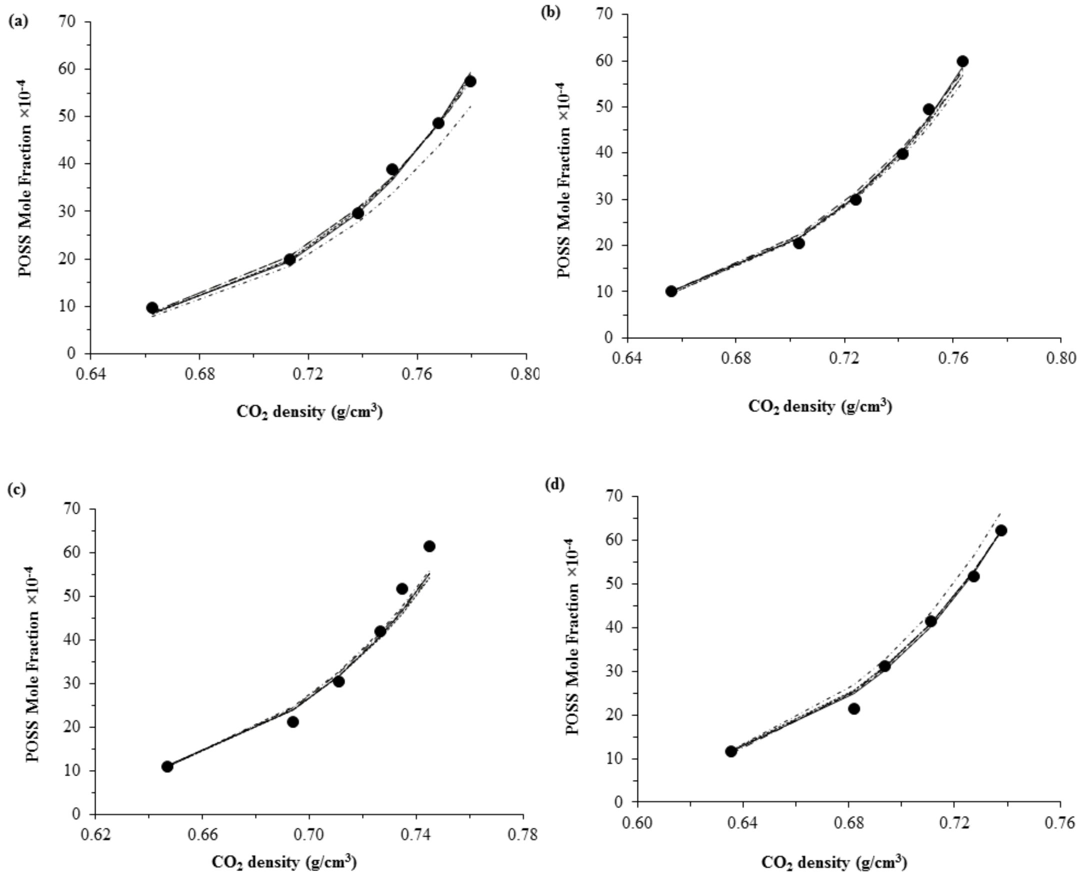

*Figure 5.8.* Density based correlations, Bartle (—·—), Chrastil (— —), MST (-----), D-A (-·-), K-J (——), C-W (—), and the experimental solubility data of MIBPOSS (●) in $scCO_2$ plotted against the $CO_2$ densities at the cloud points at (a) 308 K, (b) 313 K, (c) 318 K, and (d) 323 K.

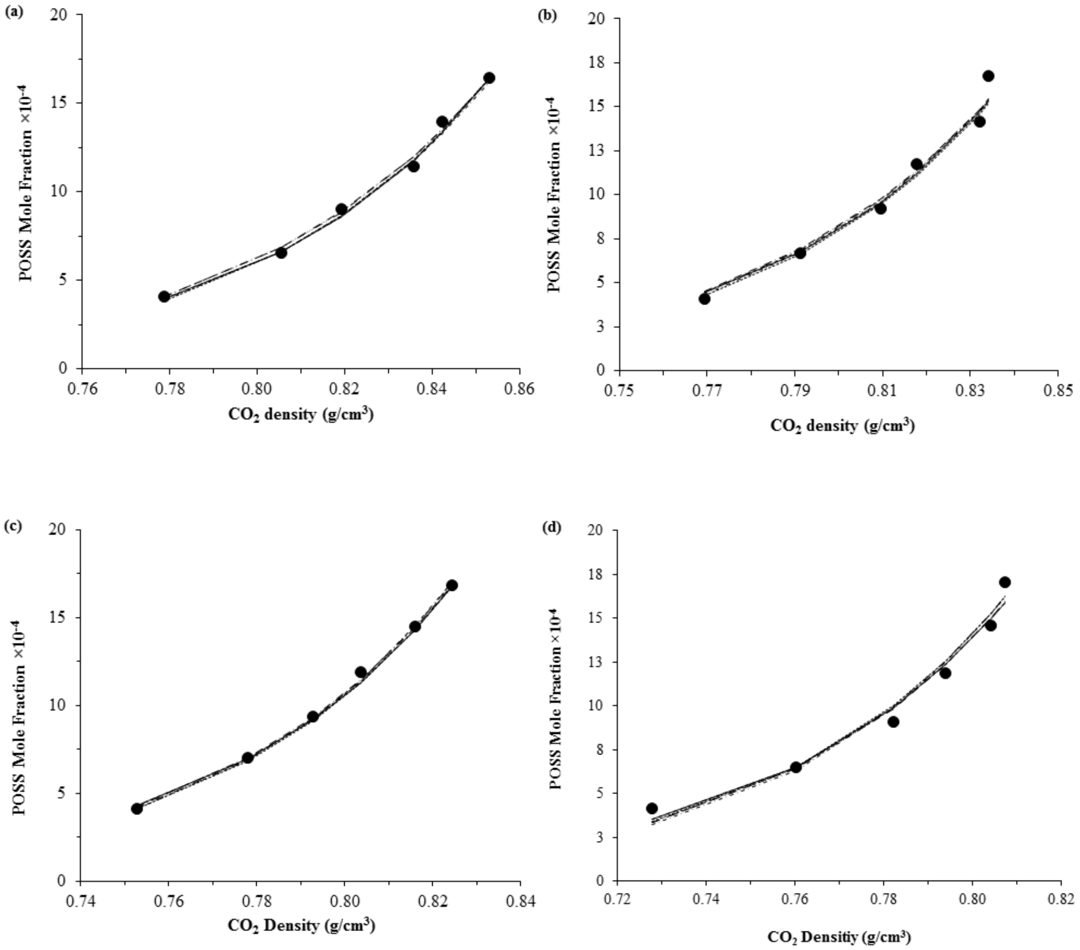

*Figure 5.9.* Density based correlations, Bartle (—·—), Chrastil (—–), MST (-----), D-A (-·-), K-J (——), C-W (—), and experimental solubility data of MIOPOSS (●) in scCO$_2$ plotted against the CO$_2$ densities at the cloud points at (a) 308 K, (b) 313 K, (c) 318 K, and (d) 323 K

The model parameters and AARD values for each model are given in Table 5.5. ARRD values are the range of 7.64 to 4.31 for MIBPOSS, while it is the range of 4.01 to 4.31 for MIOPOSS which indicate that these models exhibit good performance for the correlation of the experimental solubility data. The parameter “a” in the Bartle model is directly related to the heat of vaporization of the solute ($\Delta H_{vap}$). From Eq. 16, $\Delta H_{vap}$ were determined as 64 kJ/mol and 69 kj/mol for MIBPOSS and MIOPOSS, respectively. The higher $\Delta H_{vap}$ of MIOPOSS indicates that the solute-solute interactions of MIOPOSS are stronger than MIBPOSS, which also manifests itself as a lower solubility in scCO$_2$ compared to MIBPOSS. In order to compare the heat of vaporization calculated from the model with the actual value determined experimentally, DSC and TGA analyses were performed. For the solid POSS both of the analyses were carried out while for liquid POSS only TGA analysis could be performed due to the experimental restrictions of the DSC equipment. All the thermograms of these analyses are given in Appendix B. The DSC thermogram shows only the melting endotherm but no vaporization endotherm, while TGA of both POSS show that these components decompose before vaporization. The decomposition of MIBPOSS starts at about 300 °C, while MIOPOSS starts to decompose at about 400 °C. The enthalpy of vaporization values calculated from the models could not be verified with the experimental values since both POSS decompose before they evaporate. Therefore, only theoretical values, $\Delta H_{vap}$, calculated from the models are used for further analyses of heat of formation for which the original Chrastil equation is used. The "a" parameter in Chrastil equation which is equal to the summation of heat of vaporization and heat of solvation, was found to be -4778.7 and -5368.2 for MIBPOSS and MIOPOSS, respectively. From these values, the heat of solvation values of both components were found as -104 kj/mol and -114 kj/mol for MIBPOSS and MIOPOSS, respectively. The (absolute) heat of solvation of MIOPOSS in $scCO_2$ was calculated as a higher value than that of MIBPOSS, which was expected due to the higher molecular weight of MIOPOSS and thus it has stronger intermolecular interactions with $CO_2$. However, higher molecular weight due to longer chain length also decreases the entropy of mixing. Similarly, the lower molecular weight MIBPOSS exhibiting lower heat of solvation, has weaker intermolecular interactions with $CO_2$, while the entropy of mixing is greater due to the shorter chain length. As discussed earlier, the fact that the solubility of MIBPOSS is higher than MIOPOSS shows that the entropic contribution dominates the free energy of solvation, and thus MIBPOSS exhibits higher solubility, while MIOPOSS exhibits lower solubility in $scCO_2$. This finding is consistent with our experimental data which shows that the increased molecular weight with increasing chain length decreases the solubility of the component in $scCO_2$ showing that the entropic contribution dominates the free energy of mixing.

The model parameters given in Table 5.5 are consistent with each other as expected. For example, the calculated values of the parameter “a” in the Chrastil, d-A, K-J and Bartle are close to each other for both POSS. This value seems to be different for MST due to different expression of MST equation. If the “b” parameters in the MST is multiplied with the average temperature, which is 315.5 due to the expression of the MST model, they are close to “b” parameters of other models for both POSS. Also, the “k” parameters of Chrastil and d-A are the same parameters. Although the calculated “k” values for K-J and Bartle are consistent with each other, these calculated values are different for Chrastil and d-A as expected due to the variation of the model expressions.

Table 5.5. *The empirical parameters of the density-based models and the AARD (%) values obtained for MIBPOSS and MIOPOSS*

| **MIBPOSS** | | | | | | | | |
|---|---|---|---|---|---|---|---|---|
| **Model** | **AARD (%)** | **k** | **a** | **b** | **c** | **d** | **e** | **f** |
| Chrastil | 4.82 | 12.5 | -4778.7 | -63.2 | - | - | | |
| d-A | 7.64 | 12.6 | -5872.6 | -60.3 | 442.2 | - | | |
| K-J | 4.33 | 0.02 | -4939.3 | -1.9 | - | - | | |
| Bartle | 4.70 | 0.02 | -7715.2 | 23.2 | - | - | | |
| MST | 4.90 | 6.04 | 21.8 | -12229.7 | - | - | | |
| C-W | 4.31 | - | - | -5.2 | - | 0.28 | 0.016 | -4171.6 |
| **MIOPOSS** | | | | | | | | |
| **Model** | **AARD (%)** | **k** | **a** | **b** | **c** | **d** | **e** | **f** |
| Chrastil | 4.23 | 16.2 | -5368.2 | -88.1 | - | - | | |
| d-A | 4.31 | 16.7 | -5759.1 | -90.1 | 2501 | - | | |
| K-J | 4.03 | 0.02 | -5571.5 | -4.5 | - | - | | |
| Bartle | 4.19 | 0.02 | -8327.8 | 22.2 | - | - | | |
| MST | 4.03 | 7.59 | 23.2 | 14689.4 | - | - | | |
| C-W | 4.01 | - | - | -5.5 | - | 0.10 | 0.019 | -5314.4 |

The “self-consistency test” was investigated by Méndez-Santiago and Teja (1999) et al., where the experimental solubility data at different temperatures were plotted against the supercritical fluid density, along with the data obtained with the correlations, which construct a linear curve. The experimental data that does not deviate from the linear behavior generally shows the internal consistency of the experimental data and the capability of the models to allow sufficient interpolation or extrapolation of data [90]. The self-consistency test for the solubility of MIBPOSS and MIOPOSS in scCO2 are given in Figure 5.10 and 5.11 for each model. The self-consistency test of all the correlations obtained with the semi-empirical density-based models show that the experimental data do not deviate from the linear behavior, and thus the experimental data are internally self-consistent, while the models are capable of interpolation or extrapolation of data.

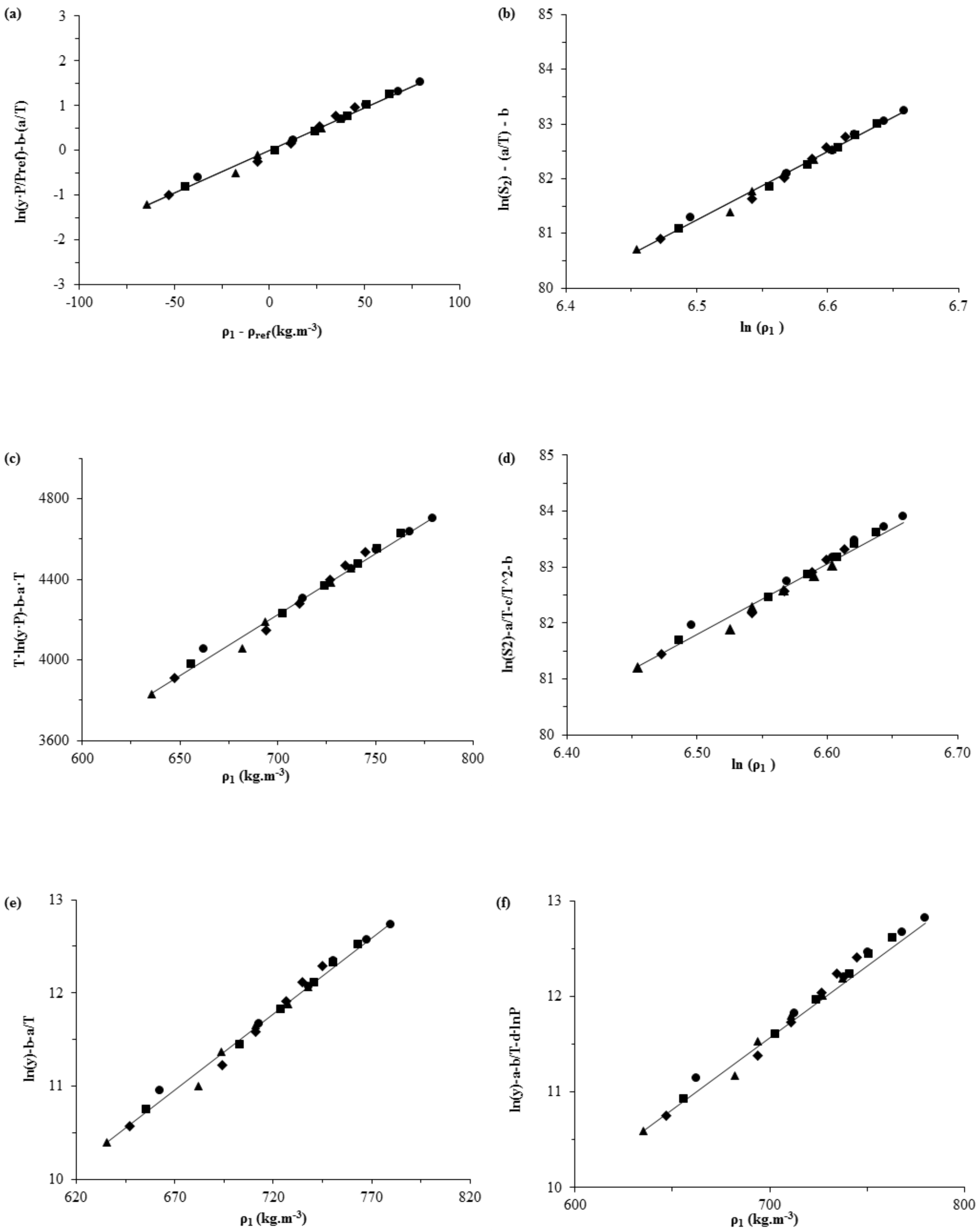

*Figure 5.10.* Self-consistency test for solubility of MIBPOSS in scCO$_2$ for each density-based model: (a) Bartle, (b) Chrastil, (c) MST, (d) D-A, (e) K-J, (f) C-W. Experimental results: 308 K (●), 313 K (■), 318 K (◆), 323K (▲), and calculated data (−)

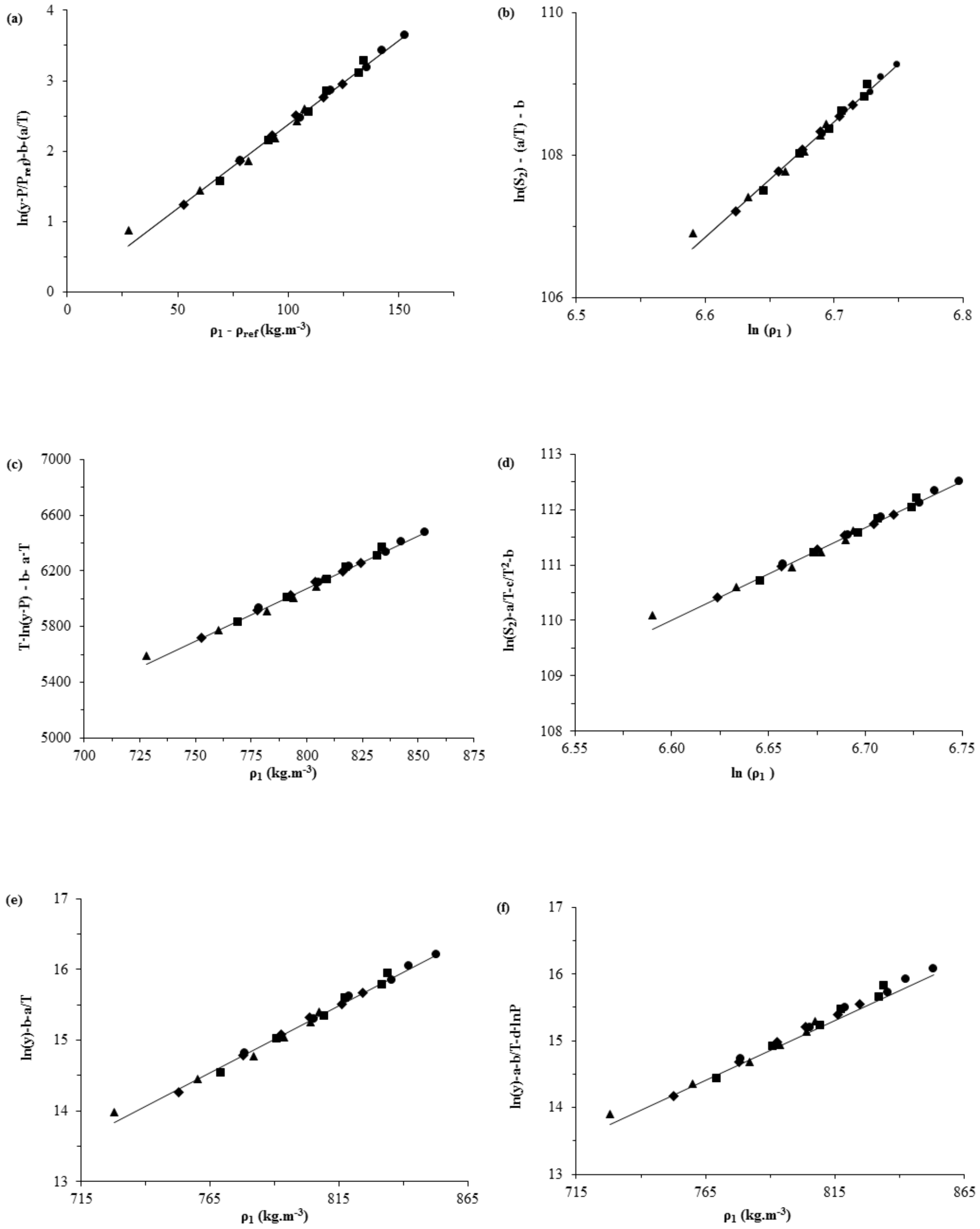

*Figure 5.11.* Self-consistency test for the solubility of MIOPOSS in scCO$_2$ for each density-based models: (a) Bartle, (b) Chrastil, (c) MST, (d) D-A, (e) K-J, (f) C-W. Experimental data: 308 K (●), 313 K (■), 318 K (◆), 323 K (▲), and calculated data (−)

## 5.4. Melting Point Depression Modelling of the Aromatic Compounds Compressed with $scCO_2$

The procedure, explained in the theoretical method section, was applied to determine the melting temperature depression of naphthalene, biphenyl and TTBB in $scCO_2$. These calculations were based on the UNIFAC model with LCVM mixing rule, and the results are presented in Table 5.7 and Figure 5.12.

Table 5.6. *Experimental and calculated melting temperature for naphthalene – $CO_2$, biphenyl – $CO_2$ and TTBB – $CO_2$ binary systems*

| **Naphthalene -$CO_2$** | | |
|---|---|---|
| **Experimental Pressure (MPa) [42]** | **Experimental Melting Temperature [42]** | **Theoretical Melting Temperature (K)** |
| 3.07 | 346.44 | 347.27 |
| 4.74 | 343.87 | 344.65 |
| 6.17 | 341.27 | 341.47 |
| 8.40 | 337.71 | 336.83 |
| 9.42 | 335.83 | 334.69 |
| 10.68 | 333.81 | 330.90 |
| 12.16 | 332.66 | 326.48 |
| **Biphenyl-$CO_2$** | | |
| **Experimental Pressure (MPa) [42]** | **Experimental Melting Temperature (K) [42]** | **Theoretical Melting Temperature (K)** |
| 2.88 | 335.7 | 337.05 |
| 4.52 | 332.02 | 333.66 |
| 5.69 | 329.61 | 330.40 |
| 7.26 | 326.48 | 325.59 |
| 8.18 | 324.53 | 322.39 |
| 9.34 | 322.84 | 319.27 |
| 10.42 | 321.97 | 316.42 |
| **TTBB-$CO_2$** | | |
| **Experimental Pressure (MPa) [74]** | **Experimental Melting Temperature (K) [74]** | **Theoretical Melting Temperature (K)** |
| 1.56 | 328.00 | 328.408 |
| 2.28 | 318.00 | 321.127 |
| 2.83 | 308.00 | 310.593 |
| 3.11 | 298.00 | 301.626 |

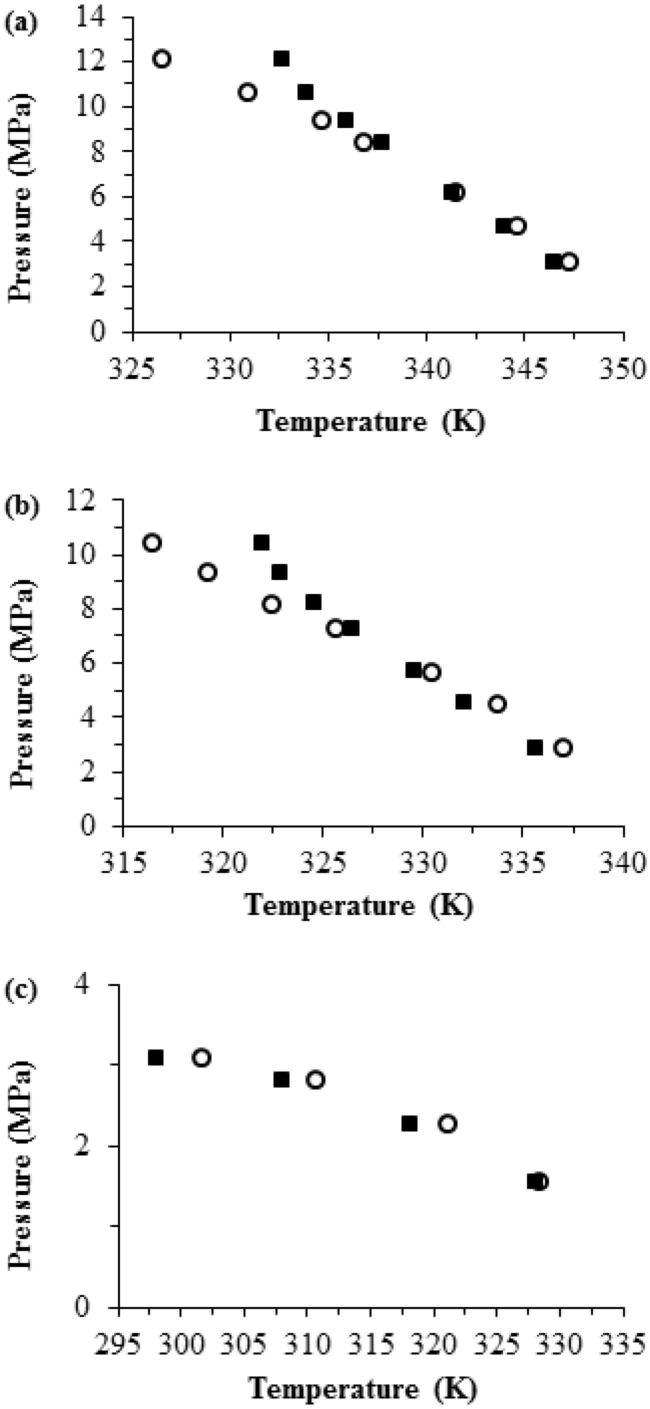

*Figure 5.12.* Experimental (■) and calculated (○) melting temperature for (a) naphthalene–$CO_2$ , (b) biphenyl–$CO_2$, and (c) TTBB-$CO_2$ binary system (Tnm=353.45 K, 342.65 K and 343 K for naphthalene, biphenyl and TTBB, respectively.)

The results showed that the UNIFAC model with the LCVM mixing rule approach gives smaller deviations at the low-pressure region than the high-pressure region for all the binary systems. In literature, similar behavior is observed for melting temperature depressions of naphthalene and biphenyl under pressurized $CO_2$ [80,91].

In order to analyze the model, different statistical parameters can be used, which are absolute average deviation of melting temperature (AADT), relative ($\Delta T\%$) and absolute average percent deviation ($|\Delta T\%|$) of the melting temperature as given in the equations, given in 37, 38 and 39 [91,92].

$$AADT = \frac{1}{n}\sum_{i=1}^{n}\left|T_i^{cal} - T_i^{exp}\right| \tag{37}$$

$$\Delta T\% = \frac{100}{n}\sum_{i=1}^{n}\left[\frac{T_i^{cal} - T_i^{exp}}{T^{exp}}\right] \tag{38}$$

$$|\Delta T\%| = \frac{100}{n}\sum_{i=1}^{n}\left[\frac{\left|T_i^{cal} - T_i^{exp}\right|}{T^{exp}}\right] \tag{39}$$

These statistical values are calculated and summarized in Table 5.8. Results of $\Delta T\%$ show that the estimated melting temperatures of naphthalene and biphenyl under pressurized $CO_2$ negatively deviate from their experimental melting temperatures while TTBB exhibits the opposite behavior. On the other hand, $|\Delta T\%|$ results show that the models give relatively similar absolute deviations for the TTBB-$CO_2$, naphthalene-$CO_2$, and biphenyl-$CO_2$ systems.

In the study of the Hong et al. [80], minimum AADT values of naphthalene and biphenyl systems were found as 4.4 K and 2 K, respectively, by using the SMS model combined with Peng Robinson EOS, while in our study, these values were calculated as 1.8476 K and 0.0069 K for naphthalene and biphenyl, respectively, which are considerably smaller than those in their study. Based on the statistical data, it can be deduced that the model can successfully estimate the melting temperature depression up to 3.11 MPa, 12.16 MPa and 10.42 MPa for TTBB, naphthalene, and biphenyl, in $CO_2$, respectively.

Table 5.7. *Calculated statistical parameters*

| | **TTBB** | **Naphthalene** | **Biphenyl** |
|---|---|---|---|
| **AADT (K)** | 2.4385 | 1.8476 | 0.0069 |
| $\Delta \boldsymbol{T}\%$ | 0.7916 | -0.4006 | -0.3750 |
| $\lvert \Delta \boldsymbol{T}\% \rvert$ | 0.7916 | 0.5512 | 0.6995 |

Both the hydrostatic pressure and solubility impacts on the melting temperature depression were investigated. In order to calculate the effects of hydrostatic pressure and solubility of $CO_2$ in the liquid phase, the terms of $\frac{T_{nm}}{\Delta H_{fus}} \Delta \vartheta_{fus} \, (P - P_0)$ and $\frac{T_{nm}}{\Delta H_{fus}} (RT \ln(\gamma_{OC} x_{OC}))$ were used, respectively. Their highest effects were calculated at the observed maximum melting point depression and given in Table 5.9. $\Delta v_{fus}$ of the compounds, given in Table 4.1, are positive, so hydrostatic pressure affects the melting temperature, positively. The results show that the hydrostatic pressure increases the melting point of naphthalene, biphenyl and TTBB up to 4.26 °C at 12.16 MPa, 4.72 °C at 10.42 MPa and 1.45 °C at 3.11 MPa, respectively. On the other hand, the solubility of compounds in the liquid phase affects the melting temperature negatively up to -31.17 °C at 12.16 MPa for naphthalene, -30.96 °C at 10.42 MPa for biphenyl and -42.83 °C at 3.11 MPa for TTBB. These results prove that the negative solubility effect is more dominant on the melting point depressions of the components than the positive effect of the hydrostatic pressure.

Table 5.8. *Calculated hydrostatic pressure and $CO_2$ solubility effects on melting temperature*

| | $x_{OC}$ | Pressure (MPa) | $\frac{T_{nm}}{\Delta H_{fus}} \Delta \vartheta_{fus} \, (P - P_0)$ | $\frac{T_{nm}}{\Delta H_{fus}} (RT \ln(\gamma_{OC} x_{OC}))$ |
|---|---|---|---|---|
| **Naphthalene** | 0.499 | 12.16 | 4.26 °C | -31.17 °C |
| **Biphenyl** | 0.514 | 10.42 | 4.72 °C | -30.96 °C |
| **TTBB** | 0.591 | 3.11 | 1.45 °C | -42.83 °C |

# CHAPTER 6

# CONCLUSIONS

In this study, the solubility and phase behavior investigations of novel material which are methacrylisobutyl POSS (MIBPOSS) and methacrylisooctyl POSS in $scCO_2$, were investigated by cloud and dew point measurement, respectively, at the temperature range of 308-323 K. Different from the other studies on the phase behavior of the POSS-$CO_2$, the studied POSS structures have two different types of functional groups attached to the Si atoms of the POSS cage structure to investigate the effects of different functional groups. The binary solid-vapor equilibrium isotherms of MIBPOSS-$CO_2$ and the binary liquid-vapor equilibrium isotherms of MIOPOSS-$CO_2$ were plotted. In the higher-pressure region, the binary systems of the POSS-$CO_2$ remain as a single homogenous continuous phase. Both solubilities of MIBPOSS and MIOPOSS in $scCO_2$ increase with pressure at isothermal conditions. On the other hand, at isobaric temperature increment, solubilities of the POSS in $scCO_2$ decrease because of the negative contribution of the density, which decreases with temperature, is more dominant than the positive contribution of the solute vapor pressure, increasing with temperature. Also, the solubility isotherms of MIBPOSS and MIOPOSS as mol fr. versus $CO_2$ density at the detected cloud, or dew points were plotted. From the graph, at constant $CO_2$ density, the solubility of POSS increases with temperature due to the increase in the vapor pressure of the POSS. The highest solubilities of MIBPOSS in $scCO_2$ were measured as 0.0062 at 16.82 MPa and 328 K while this measurement is 0.0017 at 22.06 MPa and 328 K for MIOPOSS. Also, MIBPOSS in $scCO_2$ exhibited pressure-induced melting point depression. The normal melting temperature of MIBPOSS is 385 K and it reduces to 328 K at 4.38 MPa and 308 K at 4.81 MPa.

The obtained experimental solubility data of MIBPOSS and MIOPOSS in $scCO_2$ were correlated by using Chrastil, Del Valle and Aguilera, Kumar and Johnston, Bartle, Mendez-Santiago and Teja and Chrastil modified with Wang model. AARD values of MIBPOSS are the range of 7.64 to 4.31 while it is 4.01 to 4.31 for MIOPOSS. All the models give low AARD values, thus exhibit a good correlation capability. The self-consistency tests show that the experimental data of MIBPOSS and MIOPOSS do not deviate from the solubility-density linear relation showing the internal consistency of the experimental data, and the models exhibit interpolation-extrapolation capability.

In the last part of this study, the solid-liquid equilibrium of naphthalene, biphenyl and TTBB in $scCO_2$ was investigated by modeling the melting temperature depression. Absolute average deviations of the model were 1.85 K, 0.01 K and 2.44 K for naphthalene, biphenyl and TTBB, respectively. Besides, the impact of hydrostatic pressure and the solubility on the melting temperature depression were investigated, and it was shown that the negative effect of solubility on the melting temperature depression is more dominant than the positive effect of the hydrostatic pressure.

# REFERENCES

[1] Kuo, S., & Chang, F. (2011). POSS related polymer nanocomposites, Progress in Polymer Science,36(12), 1649-1696. doi:10.1016/j.progpolymsci.2011.05.002

[2] Lligadas, G., Ronda, J. C., Galià, M., & Cádiz, V. (2006). Bionanocomposites from Renewable Resources: Epoxidized Linseed Oil−Polyhedral Oligomeric Silsesquioxanes Hybrid Materials. Biomacromolecules, 7(12), 3521-3526. doi:10.1021/bm060703u

[3] Balanuca, B., Lungu, A., Hanganu, A., Stan, L. R., Vasile, E., & Iovu, H. (2014). Hybrid nanocomposites based on POSS and networks of methacrylated camelina oil and various PEG derivatives. European Journal of Lipid Science and Technology, 116(4), 458-469. doi:10.1002/ejlt.201300370

[4] Wu, J., & Mather, P. T. (2009). POSS Polymers: Physical Properties and Biomaterials Applications. Polymer Reviews, 49(1), 25-63. doi:10.1080/15583720802656237

[5] Kanya, B., & Dilek, C. (2015). Effects of functional groups on the solubilities of polyhedral oligomeric silsesquioxanes (POSS) in supercritical carbon dioxide. The Journal of Supercritical Fluids, 102, 17-23. doi:10.1016/j.supflu.2015.03.024

[6] Ayandele, E., Sarkar, B., & Alexandridis, P. (2012). Polyhedral Oligomeric Silsesquioxane (POSS)-Containing Polymer Nanocomposites Nanomaterials, 2(4), 445-475. doi:10.3390/nano2040445

[7] Cordes, D. B., Lickiss, P. D., & Rataboul, F. (2010). Recent Developments in the Chemistry of Cubic Polyhedral Oligosilsesquioxanes. Chemical Reviews, 110(4), 2081-2173. doi:10.1021/cr900201r

[8] Li, G., Wang, L., Ni, H., & Jr., C. U. (2001). Journal of Inorganic and Organometallic Polymers, 11(3), 123-154. doi:10.1023/a:1015287910502

[9] Joshi, M., & Butola, B. S. (2004). Polymeric Nanocomposites—Polyhedral Oligomeric Silsesquioxanes (POSS) as Hybrid Nanofiller. Journal of Macromolecular Science, Part C: Polymer Reviews, 44(4), 389-410. doi:10.1081/mc-200033687

[10] Yu, J., & Qiu, Z. (2011). Preparation and Properties of Biodegradable Poly(l lactide)/Octamethyl-Polyhedral Oligomeric Silsesquioxanes Nanocomposites with Enhanced Crystallization Rate via Simple Melt Compounding. ACS Applied Materials & Interfaces, 3(3), 890-897. doi:10.1021/am1012485

[11] Liu, Y. R., Huang, Y. D., & Liu, L. (2007). Influences of MonoSilanolIsobutyl-POSS on thermal stability of polymethylsilxoane. Journal of Materials Science, 42(14), 5544-5550. doi:10.1007/s10853-006-0972-0

[12] Pellice, S. A., Fasce, D. P., & Williams, R. J. (2003). Properties of epoxy networks derived from the reaction of diglycidyl ether of bisphenol A with polyhedral oligomeric silsesquioxanes bearing OH-functionalized organic substituents. Journal of Polymer Science Part B: Polymer Physics,41(13), 1451-1461. doi:10.1002/polb.10494

[13] Zhang, W., Li, X., Guo, X., & Yang, R. (2010). Mechanical and thermal properties and flame retardancy of phosphorus-containing polyhedral oligomeric silsesquioxane (DOPO-POSS)/polycarbonate composites. Polymer Degradation and Stability, 95(12), 2541-2546. doi:10.1016/j.polymdegradstab.2010.07.036

[14] Zheng, L., Waddon, A. J., Farris, R. J., & Coughlin, E. B. (2002). X-ray Characterizations of Polyethylene Polyhedral Oligomeric Silsesquioxane Copolymers. Macromolecules, 35(6), 2375-2379. doi:10.1021/ma011855e

[15] Soh, M. S., Sellinger, A., & Yap, A. U. (2006). Dental Nanocomposites. Current Nanoscience, 2(4), 373-381. doi:10.2174/157341306778699365

[16] Olbrich, M., Punshon, G., Frischauf, I., Salacinski, H. J., Rebollar, E., Romanin, C., Seifalian, A., Heitz, J. (2007). UV surface modification of a new nanocomposite polymer to improve cytocompatibility. Journal of Biomaterials Science, Polymer Edition, 18(4), 453-468. doi:10.1163/156856207780425059

[17] Mirmohammadi, S., Imani, M., Uyama, H. and Atai, M. (2014). Hybrid Organic Inorganic Nanocomposites Based on Poly(ϵ-Caprolactone)/Polyhedral Oligomeric Silsesquioxane: Synthesis andIn VitroEvaluations. International Journal of Polymeric Materials and Polymeric Biomaterials, 63(12), pp.624 631. doi:10.1080/00914037.2013.854236

[18] Nair, B., Vaikkath, D. and Nair, P. (2013). Polyhedral Oligomeric Silsesquioxane-F68 Hybrid Vesicles for Folate Receptor Targeted Anti-Cancer Drug Delivery. Langmuir, 30(1), pp.340-347. doi: 10.1021/la4036997

[19] Alobaid, N., Salacinski, H., Sales, K., Ramesh, B., Kannan, R., Hamilton, G. and Seifalian, A. (2006). Nanocomposite Containing Bioactive Peptides Promote Endothelialisation by Circulating Progenitor Cells: An In vitro Evaluation.European Journal of Vascular and Endovascular Surgery, 32(1), pp.76-83. doi:10.1016/j.ejvs.2005.11.034

[20] Chan, K., Sonar, P. and Sellinger, A. (2009). Cubic silsesquioxanes for use in solution processable organic light emitting diodes (OLED). Journal of Materials Chemistry, 19(48), p.9103. doi: 10.1039/b909234j

[21] Sun, D., Ren, Z., Bryce, M. and Yan, S. (2015). Arylsilanes and siloxanes as optoelectronic materials for organic light-emitting diodes (OLEDs). Journal of Materials Chemistry C, 3(37), pp.9496-9508. doi:10.1039/c5tc01638j

[22] Hartmann-Thompson, C., Keeley, D., Pollock, K., Dvornic, P., Keinath, S., Dantus, M., Gunaratne, T. and LeCaptain, D. (2008). One- and Two-Photon Fluorescent Polyhedral Oligosilsesquioxane (POSS) Nanosensor Arrays for the Remote Detection of Analytes in Clouds, in Solution, and on Surfaces. Chemistry of Materials, 20(8), pp.2829 2838. doi:10.1021/cm703641s

[23] Mchugh, M. A., & Krukonis, V. J. (1994). Supercritical FIuid Extraction (2nd Edition). Butterworth-Heinemann.

[24] Knez, Ž, Markočič, E., Leitgeb, M., Primožič, M., Hrnčič, M. K., & Škerget, M. (2014). Industrial applications of supercritical fluids: A review. Energy, 77, 235-243. doi:10.1016/j.energy.2014.07.044

[25] Reichardt, C., & Welton, T. (2011). Solvents and Solvent Effects in Organic Chemistry. Weinheim: Wiley-VCH-Verl.

[26] Gopaliya, P., Kamble, P. R., Kamble, R., & Chauhan, C. S. (2014). International Journal of Pharma Research & Review, 59-66.

[27] Perrut, M. (2000). Supercritical Fluid Applications: Industrial Developments and Economic Issues. Industrial & Engineering Chemistry Research, 39(12), 4531 4535. doi:10.1021/ie000211c

[28] Raveendran, P., Ikushima, Y., & Wallen, S. L. (2005). Polar Attributes of Supercritical Carbon Dioxide. Accounts of Chemical Research, 38(6), 478-485. doi:10.1021/ar040082m

[29] Zhang, X., Heinonen, S., & Levaenen, E. (2015). ChemInform Abstract: Applications of Supercritical Carbon Dioxide in Materials Processing and Synthesis. ChemInform, 46(9). doi:10.1002/chin.201509338

[30] Tezsevin, I., Demirtas, C., Onal, I., & Dilek, C. (2017). Density functional theory study of interactions between carbon dioxide and functionalized polyhedral oligomeric silsesquioxanes. International Journal of Quantum Chemistry, 117(16). doi:10.1002/qua.25397

[31] Rawson, A., Tiwari, B. K., Brunton, N., Brennan, C., Cullen, P. J., & Odonnell, C. P. (2012). Application of Supercritical Carbon Dioxide to Fruit and Vegetables: Extraction, Processing, and Preservation. Food Reviews International, 28(3), 253-276. doi:10.1080/87559129.2011.635389

[32] Tadros, M. E., Adkins, C. L., Russick, E. M., & Youngman, M. P. (1996). Synthesis of titanium dioxide particles in supercritical $CO_2$. The Journal of Supercritical Fluids, 9(3), 172-176. doi:10.1016/s0896-8446(96)90029-7

[33] Wood, C. D., Cooper, A. I., & Desimone, J. M. (2004). Green synthesis of polymers using supercritical carbon dioxide. Current Opinion in Solid State and Materials Science, 8(5), 325-331. doi:10.1016/j.cossms.2005.02.001

[34] Davies, O. R., Lewis, A. L., Whitaker, M. J., Tai, H., Shakesheff, K. M., & Howdle, S. M. (2008). Applications of supercritical $CO_2$ in the fabrication of polymer systems for drug delivery and tissue engineering. Advanced Drug Delivery Reviews, 60(3), 373-387. doi:10.1016/j.addr.2006.12.001

[35] Montes, A., Pereyra, C., E. J. Martinez de la Ossa, & Gordillo, M. D. (2011). Particles Formation Using Supercritical Fluids. INTECH Open Access Publisher.

[36] Gupta, R. B., & Shim, J. (2007). Solubility in supercritical carbon dioxide. Boca Raton, FL: CRC Press.

[37] York, P., Kompella, U. B., & Shekunov, B. Y. (2005). Supercritical fluid technology for drug product development. New York: Informa Healthcare.

[38] Teoh, W. H., Mammucari, R., & Foster, N. R. (2013). Solubility of organometallic complexes in supercritical carbon dioxide: A review. Journal of Organometallic Chemistry, 724, 102–116. doi:10.1016/j.jorganchem.2012.10.005

[39] Burkinshaw, S. M., & Filarowski, A. (2016). Physico-chemical Aspects of Textile Coloration. John Wiley & Sons.

[40] Anastas, P. T. (2013). Handbook of Green Chemistry. Green Solvents, Supercritical Solvents (Vol. 4). Weinhem: Wiley-VCH Verlag GmbH.

[41] Lian, Z., Epstein, S. A., Blenk, C. W., & Shine, A. D. (2006). Carbon dioxide-melting point depression of biodegradable semicrystalline polymers. The Journal of Supercritical Fluids, 39(1), 107-117. doi:10.1016/j.supflu.2006.02.001

[42] Cheong, P., Zhang, D., Ohgaki, K., & Lu, B. (1986). High pressure phase equilibria for binary systems involving a solid phase. Fluid Phase Equilibria, 29, 555 562. doi:10.1016/0378-3812(86)85054-3

[43] Fukné-Kokot, K., König, A., Knez, Ž, & Škerget, M. (2000). Comparison of different methods for determination of the S–L–G equilibrium curve of a solid component in the presence of a compressed gas. Fluid Phase Equilibria, 173(2), 297-310. doi:10.1016/s0378-3812(00)00437-4

[44] Liu, J., Kim, Y., & Mchugh, M. A. (2006). Phase behavior of the vanillin–$CO_2$ system at high pressures. The Journal of Supercritical Fluids, 39(2), 201-205. doi:10.1016/j.supflu.2006.01.006

[45] Dohrn, R., Bertakis, E., Behrend, O., Voutsas, E., & Tassios, D. (2007). Melting point depression by using supercritical $CO_2$ for a novel melt dispersion micronization process. Journal of Molecular Liquids, 131-132, 53-59. doi:10.1016/j.molliq.2006.08.026

[46] Karim, A. M., Kassim, D. M., & Hameed, M. S. (2010). Phase Equilibrium Study for the Separation of Solid Components Using Supercritical Carbon Dioxide. The Open Thermodynamics Journal, 4(1), 201-211. doi:10.2174/1874396x01004010201

[47] Yeoh, H. S., Chong, G. H., Azahan, N. M., Rahman, R. A., & Choong, T. S. (2013). Solubility Measurement Method and Mathematical Modeling in Supercritical Fluids. Engineering Journal, 17(3), 67-78. doi:10.4186/ej.2013.17.3.67

[48] Sauceau, M., Letourneau, J., Richon, D., & Fages, J. (2003). Enhanced density-based models for solid compound solubilities in supercritical carbon dioxide with cosolvents. Fluid Phase Equilibria, 208(1-2), 99-113. doi:10.1016/s0378 3812(03)00005-0

[49] Škerget, M., Knez, Z., & Knez-Hrnčič, M. (2011). Solubility of Solids in Sub- and Supercritical Fluids: A Review. Journal of Chemical & Engineering Data, 56(4), 694-719. doi:10.1021/je1011373

[50] Chrastil, J. (1982). Solubility of solids and liquids in supercritical gases. The Journalof Physical Chemistry, 86(15), 3016-3021. doi:10.1021/j100212a041

[51] Tabernero, A., Melo, S. V., Mammucaric, R., Valle, E. M., & Fosterc, N. R. (2013).III Iberoamerican Conference on Supercritical Fluids.

[52] Valle, J. M., & Aguilera, J. M. (1988). An improved equation for predicting the solubility of vegetable oils in supercritical carbon dioxide. Industrial & Engineering Chemistry Research, 27(8), 1551-1553. doi:10.1021/ie00080a036

[53] Kumar, S. K., & Johnston, K. P. (1988). Modelling the solubility of solids in supercritical fluids with density as the independent variable. The Journal of Supercritical Fluids, 1(1), 15-22. doi:10.1016/0896-8446(88)90005-8

[54] Bartle, K. D., Clifford, A. A., Jafar, S. A., & Shilstone, G. F. (1991). Solubilities of Solids and Liquids of Low Volatility in Supercritical Carbon Dioxide. Journal of Physical and Chemical Reference Data, 20(4), 713-756. doi:10.1063/1.555893

[55] Méndez-Santiago, J., & Teja, A. S. (1999). The solubility of solids in supercritical fluids. Fluid Phase Equilibria, 158-160, 501-510. doi:10.1016/s0378 3812(99)00154-5

[56] Li, J., Rodrigues, M., Paiva, A., Matos, H. A., & Azevedo, E. G. (2006). Binary solid liquid–gas equilibrium of the tripalmitin/$CO_2$ and ubiquinone/$CO_2$ systems. Fluid Phase Equilibria, 241(1-2), 196-204. doi:10.1016/j.fluid.2005.12.017

[57] Prausnitz, J. M., Azevedo, E. G., & Lichtenthaler, R. N. (1999). Molecular thermodynamics of fluid-phase equilibria. New Jersey: Prentice Hall.

[58] Takebayashi, Y., Sue, K., Furuya, T., Hakuta, Y., & Yoda, S. (2014). Near-infrared spectroscopic solubility measurement for thermodynamic analysis of melting point depressions of biphenyl and naphthalene under high-pressure $CO_2$. The Journal of Supercritical Fluids, 86, 91-99. doi:10.1016/j.supflu.2013.12.007

[59] Gmehling, J., Fischer, K., Li, J., & Schiller, M. (1993). Status and results of group contribution methods. Pure and Applied Chemistry, 65(5), 919-926. doi:10.1351/pac199365050919

[60] Tosun, I. (2013). The Thermodynamics of Phase and Reaction Equilibria. Oxford: Elsevier.

[61] Gmehling, J., Kolbe, B., Kleiber, M., & Rarey, J. (2015). Chemical thermodynamics for process simulation. Weinheim: Wiley-VCH Verlag GmbH & Co. KGaA.

[62] Gorak, A., & Sørensen, E. (2014). Distillation: fundamentals and principles. Amsterdam: Elsevier.

[63] Gmehling, J. (2009). Present status and potential of group contribution methods for process development. The Journal of Chemical Thermodynamics, 41(6), 731 747. doi:10.1016/j.jct.2008.12.007

[64] Fredenslund, A., Jones, R. L., & Prausnitz, J. M. (1975). Group-contribution estimation of activity coefficients in nonideal liquid mixtures. AIChE Journal, 21(6), 1086-1099. doi:10.1002/aic.690210607

[65] Fredenslund, A., Gmehling, J., & Rasmussen, P. (1986). Vapor-liquid equilibria using UNIFAC a group contribution method. Amsterdam: Elsevier Scientific Pub. Co.

[66] Tester, J. W., & Modell, M. (2009). Thermodynamics and its applications. Bangkok: Pearson.

[67] Kontogeorgis, G. M., & Gani, R. (2004). Computer Aided Property Estimation for Process and Product Design: Computers Aided Chemical Engineering. Burlington: Elsevier Science.

[68] Orbey, H., & Sandler, S. I. (1997). A comparison of Huron-Vidal type mixing rules of mixtures of compounds with large size differences, and a new mixing rule. Fluid Phase Equilibria, 132(1-2), 1-14. doi:10.1016/s0378-3812(97)00037-x

[69] Dilek, C. (2013). Supercritical carbon dioxide-soluble polyhedral oligomeric silsesquioxane (POSS) nanocages and polymer surface modification. The Journal of Supercritical Fluids, 73, 171-177.doi:10.1016/j.supflu.2012.10.012

[70] Demirtas, C., & Dilek, C. (2019). Enhanced solubility of siloxy-modified polyhedral oligomeric silsesquioxanes in supercritical carbon dioxide. The Journal ofSupercritical Fluids, 143, 358-364. doi:10.1016/j.supflu.2018.09.015

[71] Eris, G., Sanli, D., Ulker, Z., Bozbag, S. E., Jonás, A., Kiraz, A., & Erkey, C. (2013).Three-dimensional optofluidic waveguides in hydrophobic silica aerogels via supercritical fluid processing. The Journal of Supercritical Fluids, 73, 28-33. doi:10.1016/j.supflu.2012.11.001

[72] Costeux, S., & Zhu, L. (2013). Low density thermoplastic nanofoams nucleated by nanoparticles. Polymer, 54(11), 2785-2795. doi:10.1016/j.polymer.2013.03.052

[73] Novendra, N., Hasirci, N., & Dilek, C. (2016). Supercritical processing of CO 2 –philic polyhedral oligomeric silsesquioxane (POSS)-poly( l -lactic acid) composites. The Journal of Supercritical Fluids, 117, 230-242. doi:10.1016/j.supflu.2016.06.022

[74] Dilek, C., Manke, C. W., & Gulari, E. (2008). Phase behavior of 1,3,5-tri-tert butylbenzene–carbon dioxide binary system. The Journal of Supercritical Fluids, 43(3), 421-429. doi:10.1016/j.supflu.2007.07.009

[75] Weidner, E., Wiesmet, V., Knez, Ž, & Škerget, M. (1997). Phase equilibrium (solid liquid-gas) in polyethyleneglycol-carbon dioxide systems. The Journal of Supercritical Fluids, 10(3), 139-147. doi:10.1016/s0896-8446(97)00016-8

[76] Paz, E. D., Mart.n, A., Rodríguez-Rojo, S., Herreras, J., & Cocero, M. J. (2010).Determination of Phase Equilibrium (Solid−Liquid−Gas) in Poly-(ε caprolactone)−Carbon Dioxide Systems. Journal of Chemical & Engineering Data, 55(8), 2781-2785. doi:10.1021/je900997t

[77] Kazarian, S. G., Sakellarios, N., & Gordon, C. M. (2002). High-pressure $CO_2$-induced reduction of the melting temperature of ionic liquids. Chemical Communications, (12), 1314-1315. doi:10.1039/b202759c

[78] Scurto, A. M., Newton, E., Weikel, R. R., Draucker, L., Hallett, J., Liotta, C. L., Leitner, W., & Eckert, C. A. (2008). Melting Point Depression of Ionic Liquids with $CO_2$: Phase Equilibria. Industrial & Engineering Chemistry Research, 47(3), 493 501. doi:10.1021/ie070312b

[79] Serbanovic, A., Petrovski, Ž, Manic, M., Marques, C. S., Carrera, G. V., Branco, L., C., Afonso C. A., & Ponte, M. N. (2010). Melting behaviour of ionic salts in the presence of high pressure $CO_2$. Fluid Phase Equilibria, 294(1-2), 121-130. doi:10.1016/j.fluid.2010.03.015

[80] Hong, J., Chen, H., Li, J., Matos, H. A., & Azevedo, E. G. (2009). Calculation of Solid−Liquid−Gas Equilibrium for Binary Systems Containing $CO_2$. Industrial & Engineering Chemistry Research, 48(9), 4579-4586. doi:10.1021/ie801179a

[81] E.W. Lemmon, M.O., McLinden, D.G. Friend, Thermophysical properties of fluid systems, in: P.J. Linstrom, W.G. Mallard (Eds.), NIST Chemistry WebBook, NIST Standard Reference Database Number 69, June National Institute of Standards and Technology, Gaithersburg, MD (http://webbook.nist.gov).

[82] Verevkin, S. P. (1998). Thermochemical properties of branched alkylsubstituted benzenes. The Journal of Chemical Thermodynamics, 30(8), 1029-1040. doi:10.1006/jcht.1998.0370

[83] Hansen, H. K., Rasmussen, P., Fredenslund, A., Schiller, M., & Gmehling, J. (1991). Vapor-liquid equilibria by UNIFAC group contribution. 5. Revision and extension. Ind. Eng. Chem. Res., 30(10), 2352-2355

[84] Silva, M. V., & Barbosa, D. (2004). Prediction of the solubility of aromatic components of wine in carbon dioxide. The Journal of Supercritical Fluids, 31(1), 9-25. doi:10.1016/j.supflu.2003.09.018

[85] Voutsas, E. C., Boukouvalas, C. J., Kalospiros, N. S., & Tassios, D. P. (1996). The performance of EoS/GE models in the prediction of Vapor-Liquid Equilibria in asymmetric systems. Fluid Phase Equilibria, 116(1-2), 480-487. doi:10.1016/0378-3812(95)02921-4

[86] Fink, R., Hancu, D., Valentine, R., & Beckman, E. J. (1999). Toward the Development of “$CO_2$-philic” Hydrocarbons. 1. Use of Side-Chain Functionalization to Lower the Miscibility Pressure of Polydimethylsiloxanes in $CO_2$. The Journal of Physical Chemistry B, 103(31), 6441-6444. doi:10.1021/jp990333m

[87] Nelson, M. R., & Borkman, R. F. (1998). Ab Initio Calculations on $CO_2$ Binding to Carbonyl Groups. The Journal of Physical Chemistry A, 102(40), 7860-7863. doi:10.1021/jp981824u

[88] Rindfleisch, F., Dinoia, T. P., & Mchugh, M. A. (1996). Solubility of Polymers and Copolymers in Supercritical $CO_2$. The Journal of Physical Chemistry, 100(38), 15581-15587. doi:10.1021/jp9615823

[89] Oneill, M. L., Cao, Q., Fang, M., Johnston, K. P., Wilkinson, S. P., Smith, C. D., . . . Jureller, S. H. (1998). Solubility of Homopolymers and Copolymers in Carbon Dioxide. Industrial & Engineering Chemistry Research, 37(8), 3067-3079. doi:10.1021/ie980010x

[90] Furuya, T., & Teja, A. S. (2004). The solubility of high molecular weight n-alkanes in supercritical carbon dioxide at pressures up to 50 MPa. The Journal of Supercritical Fluids, 29(3), 231-236. doi:10.1016/s0896-8446(03)00088-3

[91] Valderrama, J. O., & Arce, P. F. (2013). Modeling the melting temperature depression of ionic liquids caused by supercritical carbon dioxide. Fluid Phase Equilibria, 341, 1-6. doi:10.1016/j.fluid.2012.12.012

[92] Valderrama, J. O., & Alvarez, V. H. (2008). Correct Way of Reporting Results when Modelling Supercritical Phase Equilibria using Equations of State. The Canadian Journal of Chemical Engineering, 83(3), 578-581. doi:10.1002/cjce.5450830323

# APPENDICES

## A. Subgroup Determinations for Naphthalene, Biphenyl and TTBB

Table A.1. *Naphthalene subgroup determination*

| **Number of subgroup** | **Type of subgroup** |
|---|---|
| 8 | ACH |
| 2 | AC |

Table A.2. *Biphenyl group and subgroup determination*

| **Number of subgroup** | **Type of subgroup** |
|---|---|
| 10 | ACH |
| 2 | AC |

Table A.3. *TTBB group and subgroup determination*

| **Number of subgroup** | **Type of subgroup** |
|---|---|
| 9 | $CH_3$ |
| 3 | C |
| 3 | ACH |
| 3 | AC |

## B. Thermal Behavior of MIBPOSS and MIOPOSS

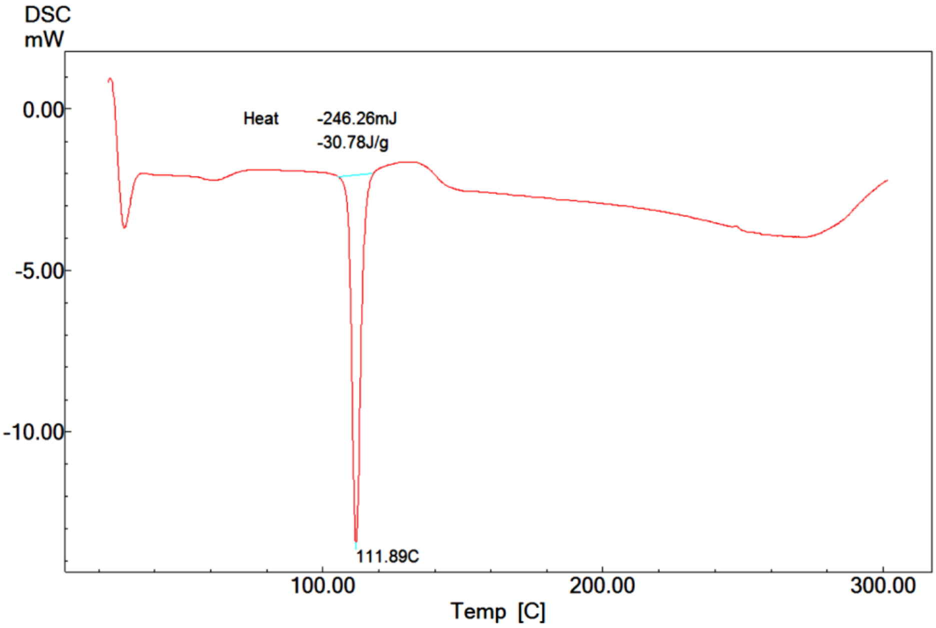

*Figure B.1. DSC analysis curve of MIBPOSS*

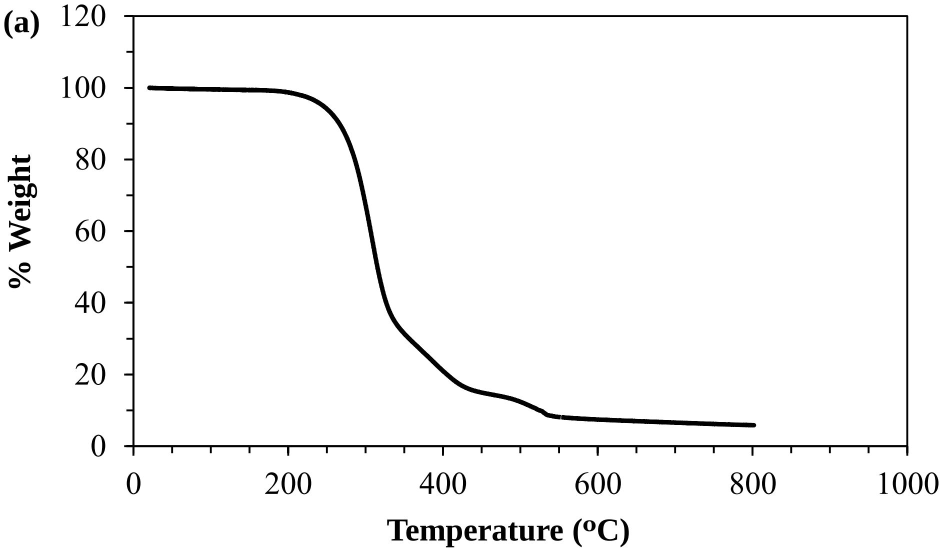

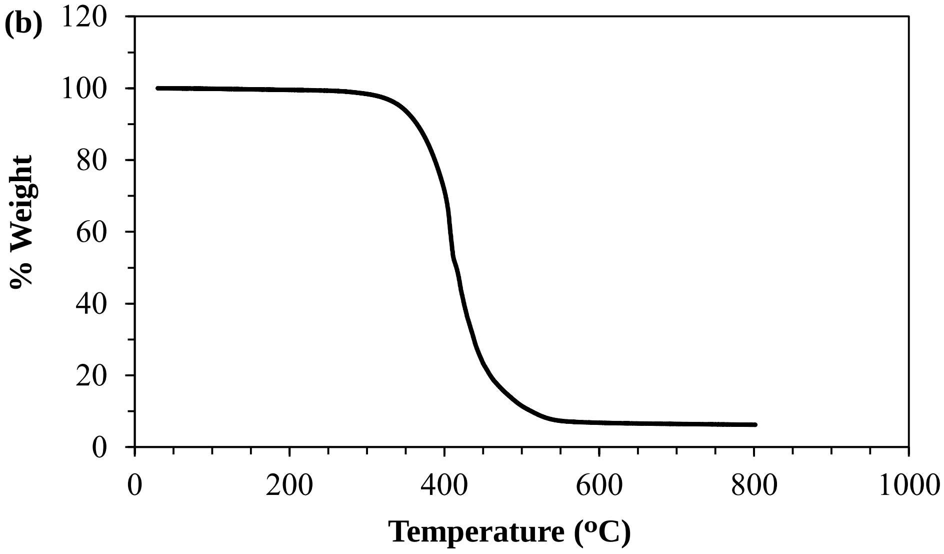

*Figure B.2. TGA analysis curve of (a)MIBPOSS and (b) MIOPOSS*